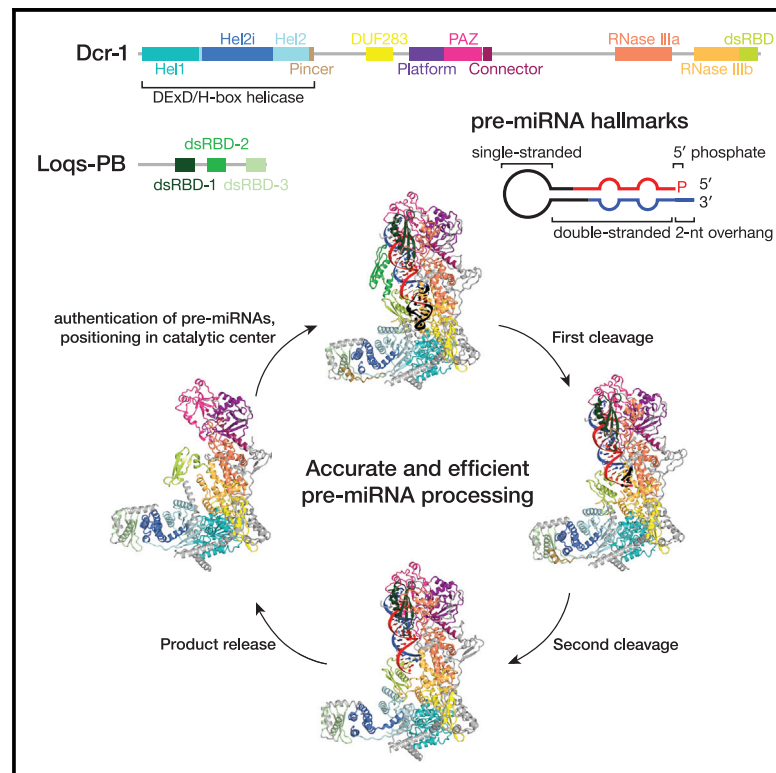# Structural basis of microRNA biogenesis by Dicer-1 and its partner protein Loqs-PB

Graphical abstract

Authors

Karina Jouravleva, Dmitrij Golovenko, Gabriel Demo, Robert C. Dutcher, Traci M. Tanaka Hall, Phillip D. Zamore, Andrei A. Korostelev

Correspondence

hall4@niehs.nih.gov (T.M.T.H.), phillip.zamore@umassmed.edu (P.D.Z.), andrei.korostelev@umassmed.edu (A.A.K.)

In brief

Six high-resolution cryo-EM structures reveal how Dicer-1—the fly homolog of mammalian Dicer—collaborates with its double-stranded RNA-binding domain partner Loquacious-PB (Loqs-PB) to validate authentic precursor-microRNA (pre-miRNAs) and to catalyze the stepwise processing of a pre-miRNA into a microRNA/microRNA* duplex ready to be loaded into an Argonaute protein.

Highlights

- Six cryo-EM structures show how fly Dicer-1 and its partner Loqs-PB make pre-miRNA

- Together, structures illustrate stepwise dicing of pre-miRNA into miRNA/miRNA* duplex

- Structures reveal how the Dicer-1·Loqs-PB heterodimer validates authentic pre-miRNAs

- Structure of the catalytically competent conformation of an animal Dicer

CellPress

Article

Structural basis of microRNA biogenesis by Dicer-1 and its partner protein Loqs-PB

Karina Jouravleva,[1,5] Dmitrij Golovenko,[1,5] Gabriel Demo,[1,2] Robert C. Dutcher,[3] Traci M. Tanaka Hall,[3,*] Phillip D. Zamore,[1,4,6,*] and Andrei A. Korostelev[1,*]

[1]RNA Therapeutics Institute, University of Massachusetts Chan Medical School, 368 Plantation Street, Worcester, MA 01605, USA
[2]Central European Institute of Technology, Masaryk University, Kamenice 5, Brno 62500, Czech Republic
[3]Epigenetics and Stem Cell Biology Laboratory, National Institute of Environmental Health Sciences, National Institutes of Health, 111 T.W. Alexander Drive, Research Triangle Park, NC 27709, USA
[4]Howard Hughes Medical Institute, University of Massachusetts Chan Medical School, 368 Plantation Street, Worcester, MA 01605, USA
[5]These authors contributed equally
[6]Lead contact
*Correspondence: hall4@niehs.nih.gov (T.M.T.H.), phillip.zamore@umassmed.edu (P.D.Z.), andrei.korostelev@umassmed.edu (A.A.K.)
https://doi.org/10.1016/j.molcel.2022.09.002

SUMMARY

In animals and plants, Dicer enzymes collaborate with double-stranded RNA-binding domain (dsRBD) proteins to convert precursor-microRNAs (pre-miRNAs) into miRNA duplexes. We report six cryo-EM structures of *Drosophila* Dicer-1 that show how Dicer-1 and its partner Loqs-PB cooperate (1) before binding pre-miRNA, (2) after binding and in a catalytically competent state, (3) after nicking one arm of the pre-miRNA, and (4) following complete dicing and initial product release. Our reconstructions suggest that pre-miRNA binds a rare, open conformation of the Dicer-1·Loqs-PB heterodimer. The Dicer-1 dsRBD and three Loqs-PB dsRBDs form a tight belt around the pre-miRNA, distorting the RNA helix to place the scissile phosphodiester bonds in the RNase III active sites. Pre-miRNA cleavage shifts the dsRBDs and partially closes Dicer-1, which may promote product release. Our data suggest a model for how the Dicer-1·Loqs-PB complex affects a complete cycle of pre-miRNA recognition, stepwise endonuclease cleavage, and product release.

INTRODUCTION

In plants and animals, microRNAs (miRNAs) direct Argonaute (AGO) proteins to repress mRNA expression by inhibiting translation or marking the RNA for destruction (Chen, 2009; Bartel, 2018; Dong et al., 2022; Zhang et al., 2022). In animals, miRNA biogenesis begins in the nucleus with the excision of a precursor-miRNA (pre-miRNA) stem loop from a primary miRNA transcript by the ribonuclease III enzyme Drosha, aided by a partner protein with multiple double-stranded RNA-binding domains (dsRBDs) (Lee et al., 2003; Denli et al., 2004; Gregory et al., 2004; Han et al., 2004, 2006). The pre-miRNA is then exported to the cytoplasm, where a second ribonuclease III enzyme, Dicer, in complex with its dsRBD-containing partner protein Loquacious in flies and TRBP or PACT in mammals, converts the pre-miRNA to a duplex comprising a miRNA guide paired to its miRNA* passenger strand (Grishok et al., 2001; Hutvágner et al., 2001; Knight and Bass, 2001; Zhang et al., 2004; Chendrimada et al., 2005; Förstemann et al., 2005; Haase et al., 2005; Maniataki and Mourelatos, 2005; Saito et al., 2005; Lee et al., 2006). The miRNA duplex is loaded into an AGO protein, and the miRNA*—the strand of the duplex equivalent to the target RNA—is evicted from the complex (Khvorova et al., 2003;

Schwarz et al., 2003; Meister et al., 2004; Okamura et al., 2004; Förstemann et al., 2007; Tomari et al., 2007; Kawamata et al., 2009). Because miRNA-guided AGO proteins find their targets via base pairing between an mRNA and a small region of sequence at the miRNA 5′ end, the seed (nucleotides g2–g8), even a single nucleotide shift in the miRNA 5′ end alters the entire repertoire of miRNA targets (Lai, 2002; Lewis et al., 2003; Brennecke et al., 2005; Chiang et al., 2010; Fukunaga et al., 2012). Thus, accurate pre-miRNA processing by Dicer is a prerequisite for miRNA function.

Dicer comprises head, core, and base superdomains (Lau et al., 2009; Wang et al., 2009; Lau et al., 2012; Taylor et al., 2013; Liu et al., 2018; Sinha et al., 2018; Wang et al., 2021; Wei et al., 2021). The head contains a PAZ domain, which binds the two-nucleotide, 3′ overhang characteristic of pre-miRNAs (Lingel et al., 2003; Song et al., 2003; Yan et al., 2003; Lingel et al., 2004; Ma et al., 2004). The pre-miRNA is cleaved by the intramolecular RNase III dimer that forms the lower half of the Dicer core (Macrae et al., 2006; MacRae et al., 2007; Park et al., 2011). The C-terminal dsRBD in the Dicer core is proposed to bind the dsRNA substrate, allowing it to engage the intramolecular RNase III dimer (Nicholson, 2014; Hansen et al., 2019). A catalytically inactive DExD/H-box helicase domain forms the Dicer base,
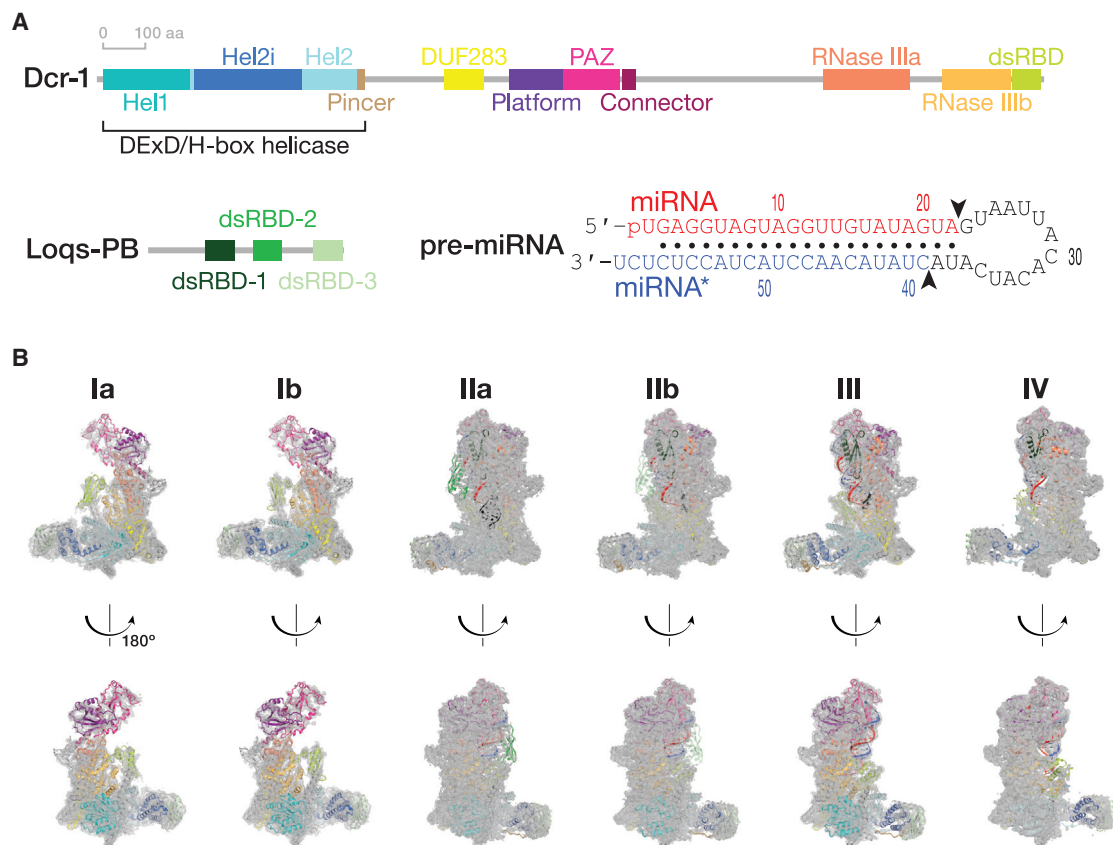
Figure 1. Cryo-EM captures Dcr-1·Loqs-PB through the cycle of processing
(A) Domain architecture of *D. melanogaster* Dcr-1 and Loqs-PB proteins and the sequence of the model pre-miRNA used for structure determination.
(B) Cryo-EM density maps (gray mesh) and the superimposed models for six states of Dcr-1·Loqs-PB alone or in complex with pre-miRNA. Domains are colored as in (A).
See also Figures S1–S4.

which recognizes the pre-miRNA loop and provides a platform to bind Dicer-partner proteins (Lee et al., 2006; Daniels et al., 2009; Cenik et al., 2011; Tsutsumi et al., 2011; Ota et al., 2013). An $\alpha\beta\beta\beta\alpha$ structural motif (domain of unknown function [DUF] 283) in the base resembles a canonical dsRBD (Gleghorn and Maquat, 2014) but binds single-stranded RNA and Dicer-partner proteins, not dsRNA (Qin et al., 2010; Ota et al., 2013; Kurzynska-Kokorniak et al., 2016).

In *Drosophila melanogaster*, Dcr-1, the ortholog of mammalian Dicer, collaborates with the dsRBD protein Loquacious to process pre-miRNAs into miRNAs (Förstemann et al., 2005; Jiang et al., 2005; Saito et al., 2005). Alternative splicing generates three *loqs* isoforms that encode Loquacious-PA (Loqs-PA), PB, and PD. Dcr-1 relies on Loqs-PA and Loqs-PB for the specific, efficient processing of pre-miRNAs (Förstemann et al., 2005; Jiang et al., 2005; Saito et al., 2005; Fareh et al., 2016). Loqs-PB enhances the dicing of pre-miRNAs containing mismatches near the scissile phosphates (Tsutsumi et al., 2011). Such mismatches promote the loading of the miRNA/miRNA* duplex into AGO for miRNAs residing on the 3′ arm of the pre-miRNA stem (Khvorova et al., 2003; Schwarz et al., 2003). Consequently,

Loqs-PB allows Dicer's preference for perfect stems to co-exist with the thermodynamic asymmetry required for the 3′ pre-miRNA arm to produce miRNAs. Loqs-PB comprises three canonical $\alpha\beta\beta\beta\alpha$ dsRBDs: the first two bind dsRNA while the third binds Dcr-1 (Figure 1A; Haase et al., 2005; Förstemann et al., 2007; Ye et al., 2007; Daniels et al., 2009; Yang et al., 2010; Wilson et al., 2015; Jakob et al., 2016).

Structures of *Giardia intestinalis* Dicer, *Drosophila* Dicer-2, and plant and human Dicers without substrate, or bound to dsRNA or pre-miRNA in an inhibited state—e.g., by substituting Ca^{2+} for Mg^{2+}—reveal the protein's overall architecture and how this protein family may bind its substrates (Macrae et al., 2006; Liu et al., 2018; Sinha et al., 2018; Wang et al., 2021; Wei et al., 2021). However, it remains unknown how Dicer proteins collaborate with their dsRNA-binding partner proteins to authenticate, bind, and cleave pre-miRNA. We used cryo-EM to visualize how *Drosophila* Dcr-1 collaborates with Loqs-PB to process pre-miRNAs. Here, we describe six structures of the Dcr-1·Loqs-PB complex alone or bound to a model pre-miRNA, at average resolutions from 3.0 to 4.0 Å (Figures 1 and S1–S4; Table S1). These structures show the stepwise mechanism of
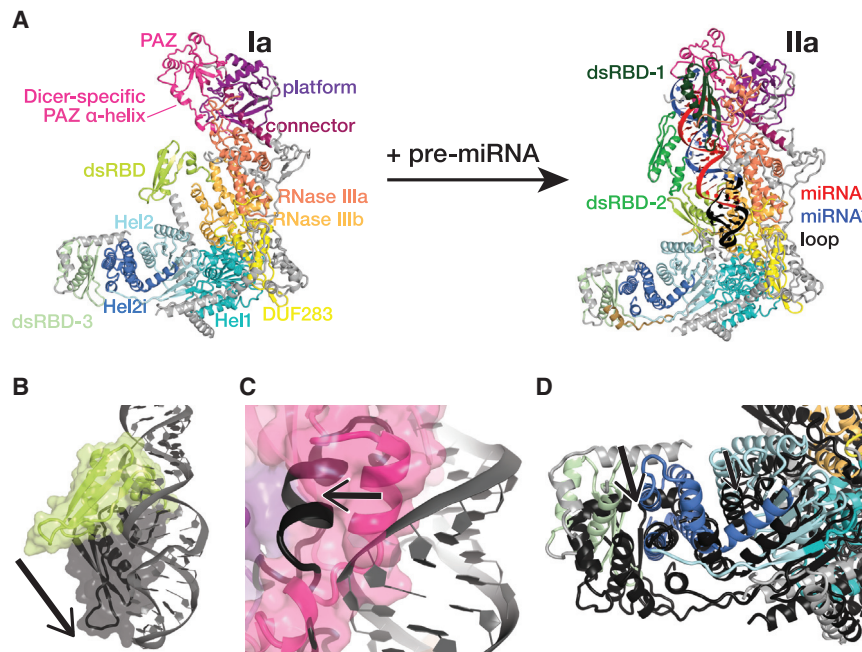
Figure 2. Dcr-1·Loqs-PB conformational equilibrium strongly favors closed states

(A) Overall views of the RNA-free Dcr-1·Loqs-PB (structure Ia) and pre-miRNA-bound Dcr-1·Loqs-PB in presence of Ca^{2+} (structure IIa).

(B–D) Close-up views showing differences in the positions of the Dcr-1 dsRBD (B), the Dicer-specific α-helix of the PAZ domain (C), and the Dcr-1 Hel2i and the Loqs-PB dsRBD-3 domains (D) between the RNA-free structure Ia (colored) and the RNA-bound structure IIa (protein domains in dark gray and pre-miRNA in gray). Structural alignments were performed by superposition of Dcr-1·Loqs-PB complexes. Black arrows highlight conformational changes upon pre-miRNA binding. See also Figure S5.

dicing, from initial substrate binding and positioning of the pre-miRNA in the two RNase III catalytic sites to the sequential hydrolysis of two phosphodiester bonds in the pre-miRNA stem and the resulting release of the diced products.

RESULTS

Ensemble cryo-EM captures Dcr-1·Loqs-PB through the cycle of pre-miRNA processing

We purified full-length Dcr-1·Loqs-PB complex from Sf9 cells and collected three cryo-EM datasets to visualize the complete cycle of pre-miRNA processing. Structures Ia and Ib correspond to ∼4.0 Å cryo-EM reconstructions of the Dcr-1·Loqs-PB complex without RNA (Figures 1 and S1–S4). Cryo-EM of the Dcr-1·Loqs-PB heterodimer with a model pre-miRNA whose miRNA resides on the 5′ arm yielded structure IIa at 3.0-Å resolution. This dataset was collected in the presence of Ca^{2+} to preserve protein-RNA interactions but inhibit dicing (Provost, 2002). Structure IIa shows the 60-nt long pre-miRNA A-form dsRNA stem and single-stranded loop bound to Dcr-1 and all three dsRBD domains of Loqs-PB. The staggered pre-miRNA cleavage sites are aligned with the two RNase III active centers, indicating that Dcr-1·Loqs-PB is poised in a cleavage-competent, pre-dicing state. Finally, cryo-EM classification of the heterodimer incubated for 5 min with pre-miRNA in the presence of Mg^{2+} at 25°C yielded an ensemble of structures that could be resolved into three distinct states, structures IIb, III, and IV. Structure IIb, a 3.3-Å reconstruction, is similar to structure IIa and corresponds to a cleavage-competent state (Figure 1B). Structure III, also at 3.3-Å resolution, lacks density for the 5′ arm of the pre-miRNA stem beyond the catalytic center of the Dcr-1 RNase IIIb domain but shows continuous density for the 3′ arm of the stem adjacent to the RNase IIIa domain. Structure III, therefore, corresponds to a nicked reaction intermediate in

which the miRNA 3′ end has been generated but the miRNA* 5′ end has not yet been produced (Figure 1B). Structure IV, a 4-Å reconstruction, lacks RNA density for both arms of the stem beyond the scissile phosphates. Structure IV represents Dcr-1·Loqs-PB after the release of the cleaved-off loop but before the release of the mature miRNA/miRNA* product (Figure 1B). Collectively, these structures illustrate the stepwise mechanism of pre-miRNA processing and suggest how Loqs-PB assists Dcr-1 to accurately and efficiently generate miRNA/miRNA* duplexes ready to load into AGO proteins.

Without pre-miRNA, Dcr-1·Loqs-PB adopts closed conformations

Structures Ia and Ib, the RNA-free Dcr-1·Loqs-PB heterodimer, display the previously defined L-shaped Dicer architecture (Figures 2A and S5A), and multiple domains of the complex share the same general topology found in *Drosophila* Dicer-2 and mammalian, Giardia, and plant Dicers (Macrae et al., 2006; Liu et al., 2018; Sinha et al., 2018; Wang et al., 2021). The core and base of Dcr-1 are well defined, but the lower resolution of the head—comprising the PAZ and platform domains—suggests that this region is dynamic without the pre-miRNA. Like the third dsRBD of TRBP—one of two Loqs orthologs in mammals (Daniels et al., 2009; Wilson et al., 2015)—the Loqs-PB dsRBD-3 binds to Hel2i of the Dcr-1 helicase domain. DsRBD-1 and dsRBD-2 of Loqs-PB are not resolved and are likely mobile. Structures Ia and Ib differ by a ∼10 Å movement of the Dcr-1 C-terminal dsRBD, which lies in different positions at the interface between the core and base in the two structures (Figure S5B). In addition, the head is shifted ∼3 Å closer to the core in structure Ia compared with Ib. Additional lower-resolution classes in this dataset revealed similar Dcr-1 conformations, with its dsRBD poorly resolved in the vicinity of the positions seen in structures Ia and Ib. These transient and less populous states, together with the highly populated conformations observed in structures Ia and Ib, all correspond to the same functional state—i.e., the protein heterodimer before substrate binding—and in solution likely interconvert.
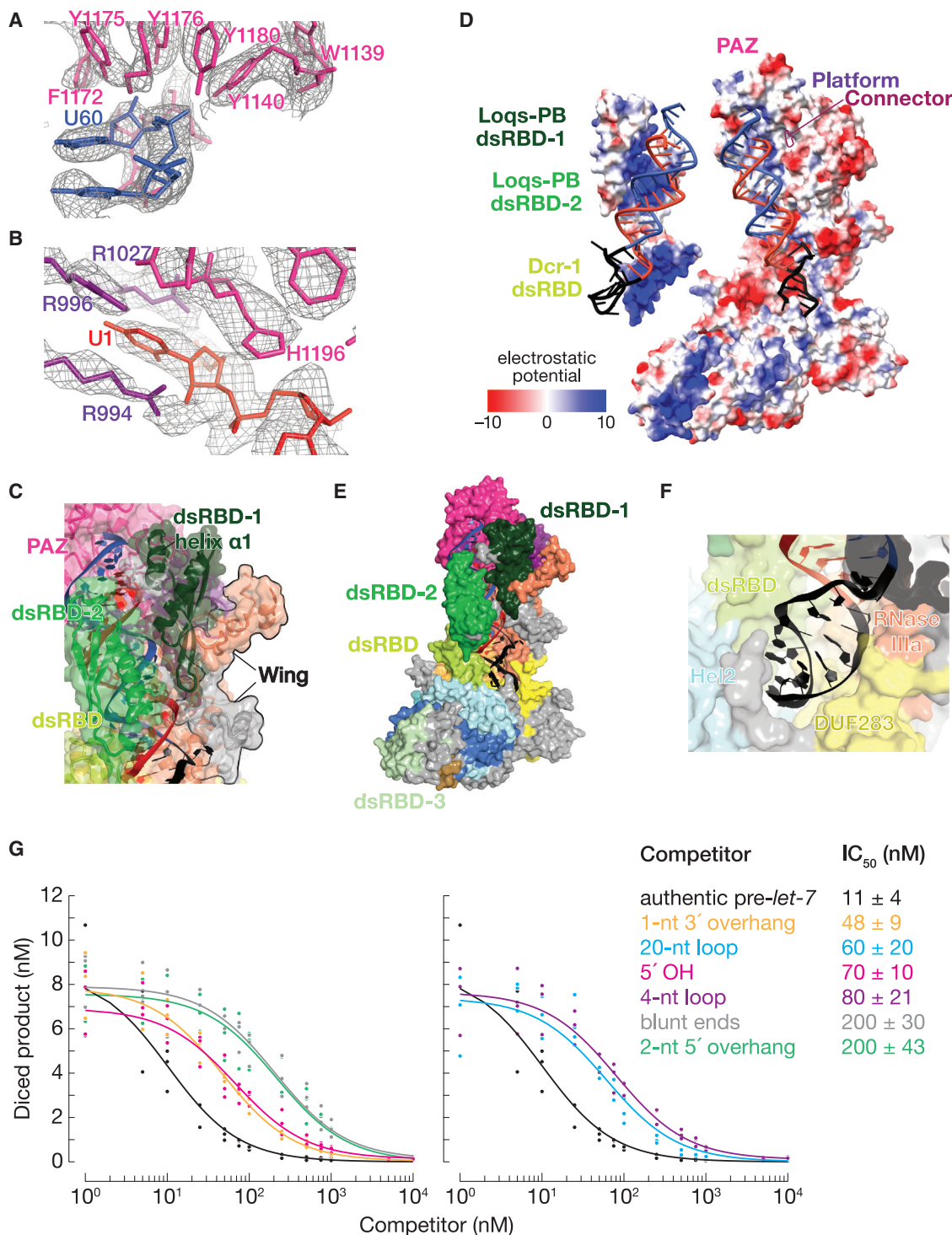
Figure 3. The Dcr-1·Loqs-PB heterodimer recognizes all four structural features of pre-miRNAs

(A and B) Cryo-EM density (mesh) of the PAZ domain pocket that binds the 3′ overhang of the pre-miRNA (A) and the binding pocket formed by the PAZ and platform domains that binds the 5′ terminal nucleotide (B). Ca^{2+} ions are shown as gold spheres.

(C) Atomic model of Dcr-1·Loqs-PB binding the stem of the pre-miRNA.

(D) Electrostatic surface view of Dcr-1·Loqs-PB; the RNA is bound in a positively charged channel. Blue, positive charge; red, negative charge.

(E) Atomic model of Dcr-1·Loqs-PB binding the single-stranded loop of the pre-miRNA.

(legend continued on next page)

The superposition of the atomic models of RNA-free Dcr-1·Loqs-PB (structure Ia) and RNA-bound Dcr-1·Loqs-PB in a catalytically competent conformation (structures IIa and IIb) reveals three major features of the apo heterodimer. First, the position of the Dcr-1 dsRBD blocks access to the RNase III active sites (Figure 2A). Second, the position of the head differs among structure Ia, structure Ib, and the RNA-bound state (Figures 2A and S5B), providing further evidence that the head is dynamic before the binding of the pre-miRNA termini to the platform and PAZ domains. In both apo structures, the Dicer-specific α-helix of the PAZ domain (aa 1,222–1,232) packs into the RNA-binding pocket, a configuration incompatible with pre-miRNA binding (Figure 2C). Third, Hel2i in the Dcr-1 base and dsRBD-3 of Loqs-PB lie >10 Å nearer to the PAZ domain in the empty heterodimer compared with the RNA-bound complex (Figure 2D). These features suggest that without RNA, the Dcr-1·Loqs-PB conformational equilibrium strongly favors closed states. Accommodation of pre-miRNA requires (1) repositioning the Dcr-1 dsRBD, (2) rearranging and stabilizing the head so that it can bind the 5′ and 3′ ends of the pre-miRNA, and (3) moving Hel2i ≥ 10 Å to widen the cleft between the core and base to accommodate the pre-miRNA loop (Figure S5C).

The Dcr-1·Loqs-PB heterodimer recognizes all of the pre-miRNA hallmark features

Structures IIa and IIb reveal how the Dcr-1·Loqs-PB heterodimer recognizes pre-miRNA. The defining features of a pre-miRNA are a two-nucleotide, single-stranded, 3′ overhanging end, a 5′-monophosphate, and a ∼22-bp double-stranded stem whose arms are linked by a single-stranded loop (Ambros et al., 2003; Park et al., 2011; Bartel, 2018). Consistent with previous biochemical and structural data (Macrae et al., 2006; Tsutsumi et al., 2011; Tian et al., 2014; Liu et al., 2018), the pre-miRNA 3′ overhang nestles in the PAZ domain (Figures 3A and S6A). To accommodate the pre-miRNA, the Dicer-specific α-helix (aa 1,222–1,232) of the PAZ domain is shifted by ∼15 Å from its position in the RNA-free structure (Figure 2C). The RNA-bound conformation of Dcr-1·Loqs-PB differs from the structures of dicing-incompetent human Dicer (Liu et al., 2018) and murine-specific, ΔHel1 DICER^O (Zapletal et al., 2022) in which the 5′ terminal phosphate and first nucleobase are disengaged from the PAZ domain. In structures IIa and IIb, the uracil of the 5′ terminal nucleotide U1 is buried in a binding pocket formed by the PAZ and platform domains, with the nucleobase stacked between Arg994 and Arg1027 (Figure 3B). The π-Arg stacking and lack of steric hindrance at the Watson-Crick face would allow binding of other 5′ nucleotides, in keeping with the occurrence of all four bases as the 5′ nucleotide of *D. melanogaster* and other Dipteran pre-miRNAs. The position of U1 differs from those in isolated PAZ:RNA crystal structures (Tian et al.,

2014), where His982 (His1196 in *D. melanogaster*) appears to block the entry of the nucleobase into the binding pocket (Figure S6A). These PAZ structures may reflect interactions sampled transiently during RNA recognition. The pre-miRNA 5′ phosphate is held in a pocket formed by the side chains of Arg1200 and Arg1207 and by the backbone amide groups of Ala1199 and Arg1200. This recognition mechanism contrasts that of plant DCL3 in which the phosphate binds a wider pocket formed by lysine side chains (Figures S6B and S6C) (Wang et al., 2021; Chen et al., 2022).

Dcr-1 recognizes the characteristic two-nucleotide, 3′ overhang of the pre-miRNA (C59-U60) using a pocket formed primarily by aromatic residues from the PAZ domain (Figure 3A). Here, the hydroxyl groups of four tyrosine side chains (Tyr1140, Tyr1175, Tyr1176, and Tyr1180) surround the U60 phosphate group, whereas the β strand at Ile1236 buttresses the U60 ribose. Moreover, PAZ and pre-miRNA interact with dsRBD-1 of Loqs-PB (Figure 3C), which likely contributes to substrate recognition and stabilization. Helix α1 of Loqs-PB dsRBD-1 (aa 135–145) packs against the minor groove of pre-miRNA helix at G4 and U58, as if constraining the pocket that binds the pre-miRNA termini. At the solvent interface, the positioning of Loqs-PB dsRBD-1 is aided by a previously unassigned subdomain of RNase III, which we term the "wing" (aa 924–957 and 1,815–1,890; Figure 3C).

The phosphate backbone of the pre-miRNA stem interacts with the positively charged protein extension formed by the platform, PAZ, and connector domains until it reaches the catalytic center of Dcr-1 (Figure 3D). On the solvent-exposed side, pre-miRNA is bound to dsRBD-2 of Loqs-PB and the dsRBD of Dcr-1 (Figure 3C). Their positively charged surfaces envelop the pre-miRNA (Figure 3D) as if forming a tight belt that helps to position pre-miRNA in the twin catalytic centers formed by the Dcr-1 intramolecular RNase III dimer (Figure 3E). The binding of the pre-miRNA by tandem dsRBDs—the Dcr-1 dsRBD and dsRBD-2 of Loqs-PB—mirrors the function of the two C-terminal dsRBD domains of *Arabidopsis* DCL3, which produces 24 nt siRNAs from dsRNA (Wang et al., 2021), and of the belt and C-terminal dsRBD domains of Drosha, which produces pre-miRNAs from primary transcripts (Figure S6D; Partin et al., 2020). The Dcr-1 dsRBD is shifted by 10 Å from its position in the RNA-free complex and is wedged between the Dcr-1 core and base, stabilizing the pre-miRNA-bound, open conformation (Figures 2A, 2B, and S5C). Finally, Loqs-PB dsRBD-3 binds to Hel2i of the Dcr-1 helicase domain and fastens the Loqs-PB belt around the substrate RNA (Figures 2A and 3E), thus stabilizing and positioning pre-miRNA for cleavage.

The pre-miRNA single-stranded loop (A25–A33) reposes in a pocket formed by the N terminus and core, base, helicase, DUF283, RNase IIIa, and the dsRBD domains of Dcr-1

(F) Structure of Dcr-1·Loqs-PB·pre-miRNA complex showing multiple domains of Dcr-1 and Loqs-PB enveloping the pre-miRNA. Protein in surface view; RNA in cartoon view. All panels correspond to structure IIa.

(G) Authentic, 5′ ^{32}P-radiolabeled pre-*let-7* (25 nM) was incubated with Dcr-1·Loqs-PB (5 nM) for 15 min in presence of increasing concentrations of hairpin RNAs, then analyzed by denaturing gel electrophoresis and quantified. The product formed as a function of competitor concentrations is shown for three independent trials. Data were fitted to a 3-parameter inhibition model $y(x) = y_{max} + \frac{y_{min} - y_{max}}{1 + IC_{50}/x}$ to obtain the IC_{50} values. Data are mean ± SD for three independent trials.

See also Figure S6.

(Figure 3F). The Hel1 region of the Dcr-1 helicase domain does not directly interact with the pre-miRNA loop but does support the arrangement of Hel2, DUF283, and RNase IIIa domains. This critical role for Hel1 may explain why its deletion in mouse Dicer leads to widespread somatic changes in the abundance and sequence of miRNAs and increased processing of non-canonical pre-miRNAs with long stems or loops (Zapletal et al., 2022). The cryo-EM structure of murine oocyte-specific Dicer^O, which lacks Hel1, shows poor density for the helicase and DUF283 domains (Zapletal et al., 2022), perhaps because mouse Hel1 similarly stabilizes the arrangement of the mouse Hel2, DUF283, and RNase IIIa domains.

Although the overall shape of the pre-miRNA loop is visible in our cryo-EM density, the unambiguous assignment of nucleotide conformations is difficult. The lower resolution of the loop versus the stem is likely due to conformational flexibility, reflecting the ability of Dcr-1 to bind loops of varying sequences and structures. The loop lies in between the Dcr-1 DUF283 (at Arg837 and Pro837) and the Dcr-1 dsRBD (at Pro2196, Tyr2224, and Arg225). These protein domains appear to provide stacking and electrostatic support for loop nucleotides without necessitating base specificity (Figure 3F). Together, our data show that the Dcr-1·Loqs-PB heterodimer recognizes all four structural features of pre-miRNAs.

To test the ability of Dcr-1·Loqs-PB to discriminate between authentic substrates and other hairpins, we performed competition assays using five pre-*let-7* variants: (1) bearing a 5′ OH instead of a phosphate moiety; with (2) a 2 nt 5′ overhang, (3) blunt ends, or (4) a 1 nt 3′ overhang instead of the canonical 2 nt 3′ overhang; or (5) a 4-nt loop in place of the natural 14-nt loop. For each competitor RNA, we measured the dicing of 5′ ^{32}P-radiolabeled authentic pre-*let-7* by the Dcr-1·Loqs-PB complex in the presence of increasing concentrations of unlabeled competitor and calculated its IC_{50} (Figure 3G). All of the hairpins lacking a canonical pre-miRNA feature had larger IC_{50} values than pre-*let-7* itself, suggesting that they bind more weakly than the authentic substrate. Therefore, we propose that binding the pre-miRNA stabilizes the open—i.e., catalytically competent—conformation of the Dcr-1·Loqs heterodimer, which our data suggest is poorly populated in the absence of RNA. Our data suggest that only when bound by pre-miRNA is the open conformation more stable than the closed, catalytically incompetent state. The role of substrate binding in stabilizing the open conformation thus enables the Dcr-1·Loqs-PB heterodimer to reject inauthentic stem-loop RNAs: such near-cognate substrates bind too weakly to shift the conformational equilibrium from a closed to an open state.

Dcr-1 and Loqs-PB position the pre-miRNA in the catalytic center

As in other eukaryotic RNase III enzymes, including human Dicer, human Drosha, *Drosophila* Dicer-2, *Giardia intestinalis* Dicer, and *Arabidopsis* DCL-1 and DCL-3, the Dcr-1 RNase III domains form an intramolecular dimer (Figures 2A and S7A) (Zhang et al., 2004; Macrae et al., 2006; Kwon et al., 2016; Liu et al., 2018; Sinha et al., 2018; Wang et al., 2021; Wei et al., 2021). In structures IIa and IIb, the two catalytic sites flank the minor groove of the pre-miRNA and interact with both arms of the pre-miRNA

stem, confirming that they correspond to cleavage-competent complexes. The conserved RNase IIIa (Glu1745, Asp1749, Asp1905, and Glu1908) and RNase IIIb (Glu2032, Asp2036, Asp2136, and Glu2139) catalytic quartets each coordinate Ca^{2+} ions in structure IIa (Figures 4A and 4B). Ca^{2+} likely neutralizes electrostatic repulsion between the enzyme and pre-miRNA, promoting stable binding but inhibiting cleavage.

Our data reveal that Loqs-PB and Dcr-1 collaborate to position the pre-miRNA into the RNA-processing center. In structures IIa and IIb, two sets of Loqs-PB and Dcr-1 interactions stabilize the pre-cleavage state of pre-miRNA. First, dsRBD-1 of Loqs-PB is docked onto the Dcr-1 RNase IIIa (Figure 3E). Specifically, the tip (Leu155–Ile162) of the β sheet of Loqs-PB dsRBD-1 packs against the small β sheet formed by the Dcr-1 RNase IIIa (in the vicinity of Ile1898) and wing (in the vicinity of Arg952 and Tyr954) (Figure 4C). The interaction of the RNA-bound domain of Loqs-PB with the RNase domain of Dcr-1 stabilizes the upper part of the RNA stem near the active sites (Figure 4B). Second, the Loqs-PB dsRBD-2 and the Dcr-1 dsRBD stabilize the lower part of the pre-miRNA stem by interacting with two consecutive minor grooves of the 21-bp stem (Figures 4D and 4E). Lys301, Lys302, and Lys305 of the evolutionarily conserved KKxAK motif of the Loqs-PB dsRBD-2 recognize the phosphate backbone of the pre-miRNA stem. The 5′ arm of the stem is further positioned by positively charged Dcr-1 residues that form salt bridges with the backbone phosphates of pre-miRNA A22 (with Arg2225) and G20 (with Lys2228) and by the side chain of Dcr-1 residue Ile2180, which packs against the ribose sugar of nucleotide A19 (Figure 4E). Loop adenosine A36, which lies two nucleotides 3′ to the scissile phosphate of the 5′ arm of the stem, is bulged out and supported by a π-cation interaction with Arg945 of Dcr-1 (Figure 4F). Loop nucleotides guanosine G23 and cytosine C35 form a canonical Watson-Crick base-pair, and uracils U24 and U34 form a non-canonical Watson-Crick-like base-pair, extending the pre-miRNA stem and directing the pre-miRNA loop into the loop-binding pocket of Dcr-1 (Figure 4F). Together, these contacts position the pre-miRNA stem in the dicing center and stabilize the displacement of the scissile phosphate at the 3′ end of the prospective miRNA by 4 Å and at the 5′ end of the future miRNA* by 3 Å relative to their positions in an A-form helix (shown by arrows in Figure 4D). This displacement moves the scissile phosphates into the RNase IIIb and IIIa active sites, achieving a catalytically competent geometry (Figures 4D and 5A).

The requirement for distortion of the A-form helix for the substrate to engage the active sites may increase the substrate specificity of the enzyme. To test this idea, we designed pre-*let-7*-like hairpins with RNA stems containing nearest neighbor pairs selected to increase inter-base-pair stacking energy (Saenger, 1984; Xia et al., 1998), the main determinant of the rigidity of a nucleic acid helix. We used the competition assay to measure their IC_{50} values (a measure of binding affinity) and dicing assays to determine the concentration of the active enzyme formed for each substrate. All of these competitor hairpins displayed IC_{50} values similar (≤1.7-fold change from pre-*let-7* itself) to that of authentic pre-*let-7*: they all bind tightly to Dcr-1·Loqs-PB (Figure S7B). Yet, the concentration of active enzyme E_{active} declined with increasing stem stability, ΔG_{stem}
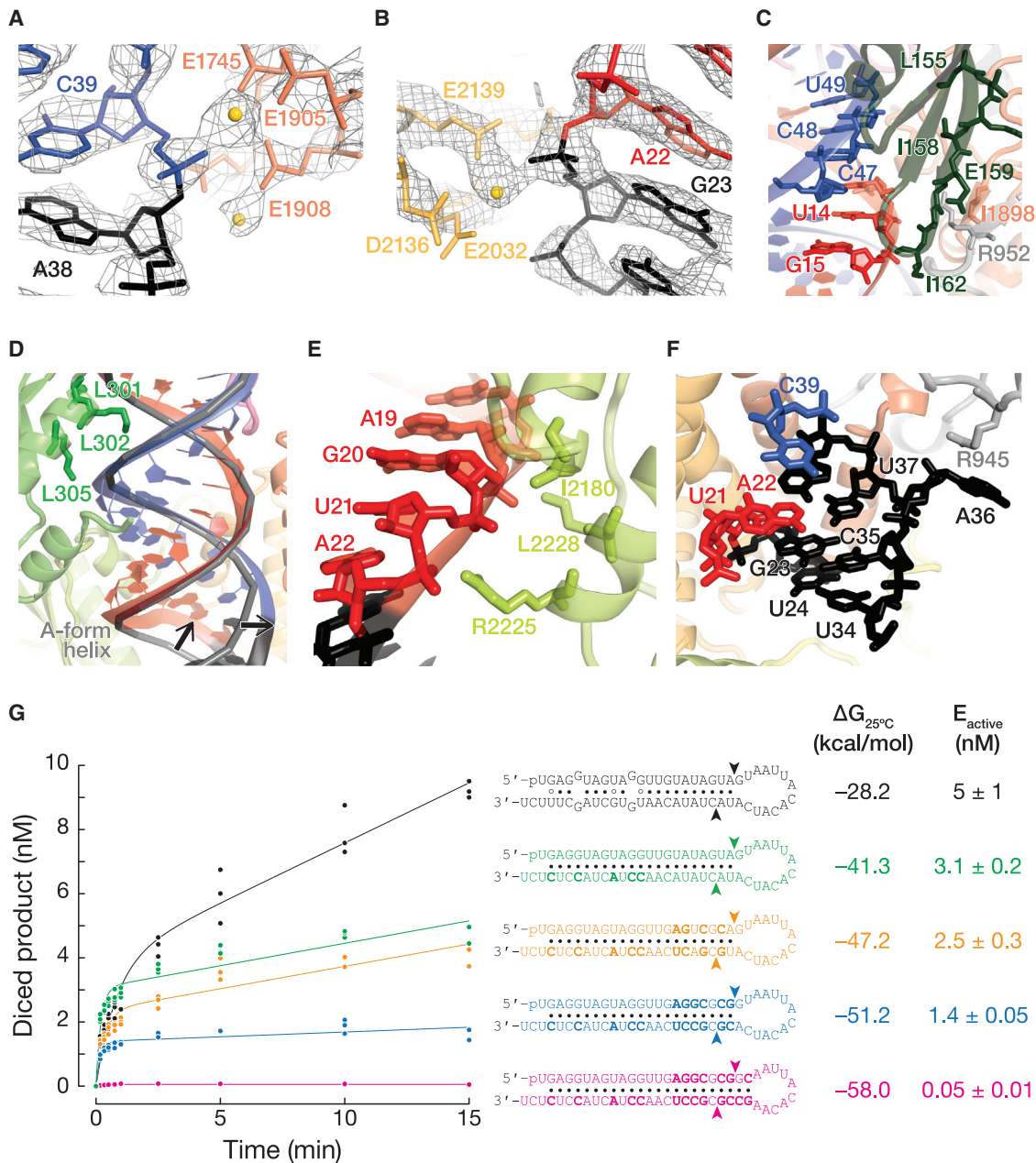
Figure 4. Dcr-1 and Loqs-PB position the pre-miRNA in the dicing center

(A and B) Cryo-EM density (mesh) of RNase IIIa (dark orange) (A) and RNase IIIb (light orange) (B) active site residues in the pre-miRNA-bound Dcr-1·Loqs-PB complex (structure IIa). Gold spheres: Ca^{2+} ions.

(C) Cartoon representation of dsRBD-1 of Loqs-PB (dark green) and the Dcr-1 wing (gray and orange) stabilizing the upper part of the RNA stem. Interacting residues are shown as sticks.

(D and E) Cartoon representation of dsRBD-2 of Loqs-PB (D) and the dsRBD of Dcr-1 (E) stabilizing the lower part of the pre-miRNA stem. DsRBD-2 of Loqs-PB and the Dcr-1 dsRBD are shown in green and lime green, respectively. A perfect A-form helix (predicted by RNAComposer) has been superposed as a gray ribbon. Black arrows indicate the displacement of the pre-miRNA 5′ arm by 4 Å and of the 3′ arm by 3 Å relative to their positions in an A-form helix.

(F) Cartoon representation of the extended pre-miRNA lower stem. Adenosine A36 is bulged out and supported by a π-cation interaction with Arg945 of Dcr-1 (gray). All panels correspond to structure IIa.

(G) Authentic, 5′ ^{32}P-radiolabeled pre-*let-7* and pre-*let-7*-like hairpins (16 nM) were incubated with 4 nM Dcr-1·Loqs-PB, then analyzed by denaturing gel electrophoresis and quantified. The product formed as a function of time is shown for three independent trials. Data were fitted to the burst-and-steady-state equation (STAR Methods), which enables estimating the concentration of the active enzyme, E_{active}.
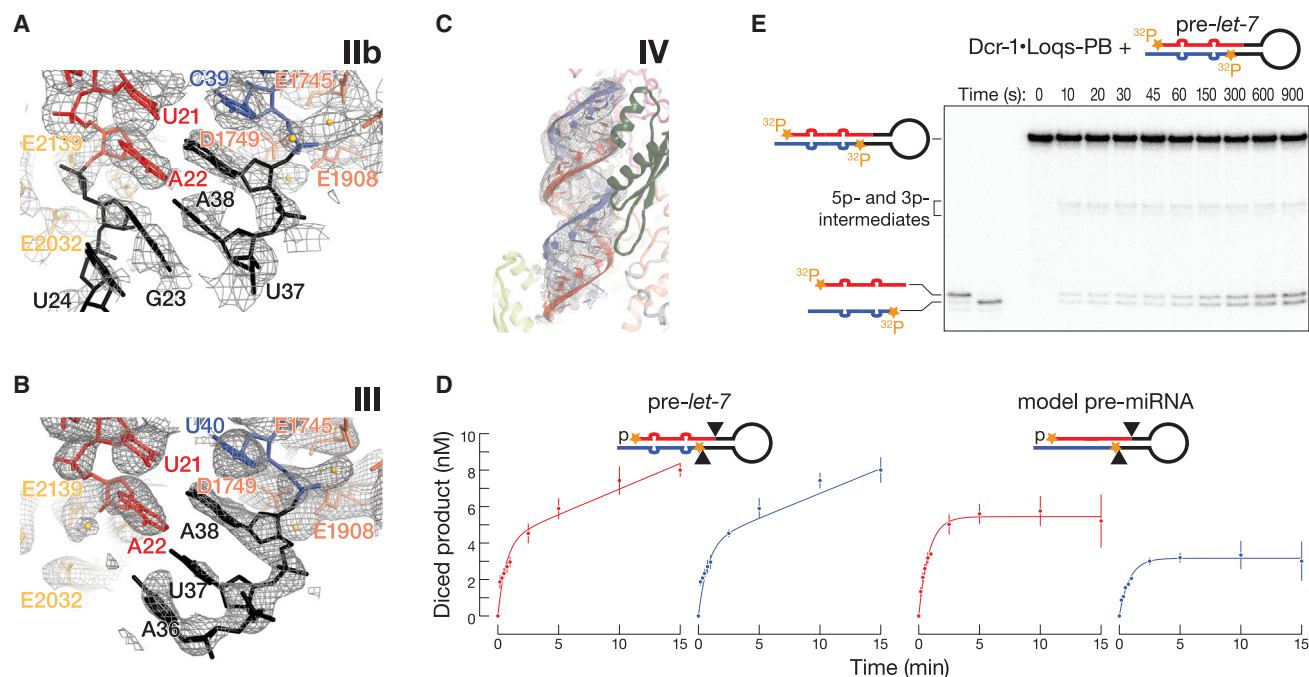
See also Figure S7.

Figure 5. Cleavage of the pre-miRNA stem

(A and B) Cryo-EM density (mesh) of RNase IIIa and RNase IIIb active centers of RNA-bound Dcr-1·Loqs-PB complex in structure IIa (A) and III (B). The residues composing the catalytic RNase IIIa and RNase IIIb sites are shown in dark and light orange, respectively. Gold spheres: Ca^{2+} ions.

(C) Cryo-EM density (mesh) corresponding to the miRNA/miRNA* duplex seen in structure IV in which both arms of the pre-miRNA stem have been cleaved. Superposed is the model of Dcr-1·Loqs-PB·pre-miRNA shown in cartoon representation.

(D) Authentic pre-*let-7* and model pre-miRNA were radiolabeled with two ^{32}P (orange). Substrate RNAs (45 nM) were incubated with 5 nM Dcr-1·Loqs-PB, then diced products generated from 5′ and 3′ arms (red and blue, respectively) were analyzed by denaturing gel electrophoresis and quantified. Data were fitted to the burst-and-steady-state equation (STAR Methods). Data are mean ± SD for three independent trials.

(E) Representative denaturing polyacrylamide gel image for pre-*let-7* cleavage by Dcr-1·Loqs-PB.

(Figure 4G). Because we used the same preparation of Dicer-1·Loqs PB in all of these experiments, differences in the concentration of active enzyme must therefore correspond to different concentrations of catalytically competent enzyme:substrate complex for the hairpins of different thermodynamic stabilities (Sassa et al., 2013). These data support the idea that substrate binding to the open conformation of the enzyme is unlikely to be sufficient for dicing. Instead, the substrate must also be able to be distorted to fit the active sites, a conformational change that becomes more difficult as the stability or length of the stem increases.

Cleavage of the 5′ and 3′ arms of the pre-miRNA stem

RNase III enzymes cleave each RNA strand via a bimolecular nucleophilic substitution mechanism that requires two Mg^{2+} ions and leaves 3′-hydroxyl and 5′-monophosphate product termini (Dunn, 1982; Blaszczyk et al., 2001; Hutvágner et al., 2001; Campbell et al., 2002; Sun et al., 2005; Gan et al., 2008; Court et al., 2013; Nicholson, 2014). Structures IIa and IIb are consistent with this mechanism, and both the Ca^{2+} (structure IIa) and Mg^{2+} (structure IIb) structures reveal a pair of divalent cations in the RNase IIIa active site (Figures 4A and 5A). A single Ca^{2+} ion was well resolved in RNase IIIb active site, whereas weaker density suggests that the second ion may be bound with partial occupancy (Figure 4B).

In structure III, the RNase IIIa domain binds the 3′ arm of the pre-miRNA: two Mg^{2+} ions are coordinated in the active site. Strong density indicates that the 3′ arm is intact and extends past the cleavage site between nucleotides A38 and C39. By contrast, no RNA density is observed in the RNase IIIb active site for the 5′ arm beyond nucleotide A22, suggesting that the 5′ arm has been cleaved and that the loop still attached to the 3′ arm of the stem has left the RNase IIIb active site and is mobile (Figure 5B). Structure III, therefore, represents the Dcr-1·Loqs-PB heterodimer bound to a pre-miRNA in which the 3′ end of the miRNA on the 5′ arm has been defined but the 3′ arm remains to be cut. In contrast to structure III, both arms of the stem are diced in structure IV, producing a miRNA/miRNA* duplex product with two 3′ overhanging nucleotides at each end (Figure 5C). Maximum-likelihood classification of the cryo-EM dataset detected no RNA-free Dcr-1·Loqs-PB complexes. Moreover, the high IC_{50} value (900 ± 200 nM) of the miRNA/miRNA* duplex in our dicing competition experiments suggests that the Dcr-1·Loqs-PB has a low affinity for its product (Figure S7B). Together, these data support the idea that structure IV represents the Dcr-1·Loqs-PB complex prior to the release of the miRNA/miRNA* duplex, rather than after release and rebinding. Maximum-likelihood classification of the cryo-EM dataset detected no structures with an intact 5′ arm and a cleaved 3′ arm, suggesting that processing of
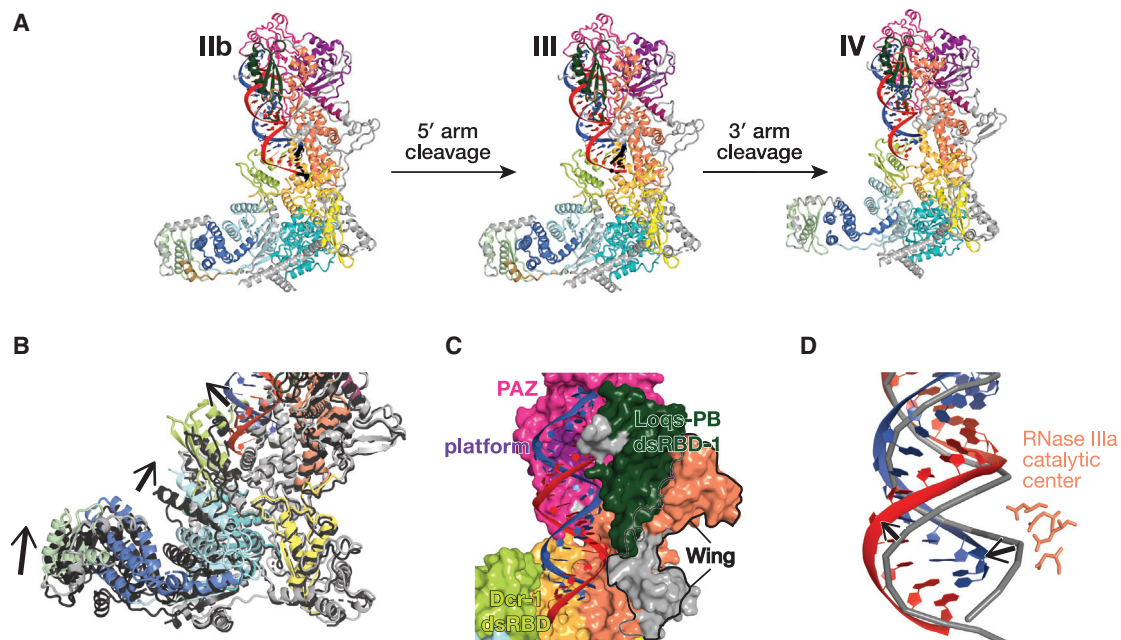
Figure 6. Conformational transitions define ordered product release

(A) Overall views of the pre-miRNA-bound Dcr-1·Loqs-PB complex in presence of Mg^{2+} before cleavage (structure IIb), after cleavage of the 5′ arm of the model pre-miRNA (structure III), and after cleavage of both the 5′ and 3′ arms (structure IV).

(B) Close-up view showing differences in the positions of the Dcr-1 dsRBD and Hel2i domains and the Loqs-PB dsRBD-3 in the Dcr-1·Loqs-PB·pre-miRNA structure IV after both 5′ and 3′ arms of the pre-miRNA have been cleaved (red and blue) relative to those in structure III after cleavage of the 5′ arm of the model pre-miRNA (protein domains in dark gray). Structural alignments were performed by superposition of Dcr-1·Loqs-PB·pre-miRNA complexes. Black arrows indicate conformational changes upon the second cleavage event.

(C) Structure of Dcr-1·Loqs-PB·pre-miRNA complex in surface (protein) and cartoon (RNA) views, showing the mature miRNA/miRNA* duplex remaining anchored to the Dcr-1 PAZ and platform domains.

(D) Superposition of atomic models of mature duplex (structure IV) and pre-miRNA (structure IIb), showing the lower part of the duplex (red and blue) shifted ∼5 Å from its position before cleavage (gray). RNA shown in cartoon representation. RNase IIIa catalytic center (structure IV) shown as sticks.

the model pre-miRNA is predominantly sequential, with the 5′ arm being cleaved first. In agreement with this idea, the rate of 5′ arm cleavage was faster than the rate of 3′ arm cleavage for the model pre-miRNA (Figure 5D). We note that cleavage of pre-*let-7* generates *let-7* (5′ arm) and *let-7** (3′ arm) with identical rates (Figures 5D and 5E) and is unlikely to follow a specific order of cleavage.

Pre-miRNA cleavage allows conformational transitions that define the order of product release

Cleavage of the 5′ arm of the model pre-miRNA does not alter the structure of Dcr-1 from its RNA-bound, pre-cleavage state. Similarly, the Loqs-PB dsRBD-1 and dsRBD-3 domains do not move relative to Dcr-1 between structure IIb and III (Figure 6A). By contrast, the Loqs-PB dsRBD-2, which is well resolved in structure IIa and partially resolved in IIb, is not visible in structure III (Figures 1B, 2A, and 6A), suggesting that it becomes mobile upon cleavage of the 5′ arm and loses its interaction with the Dcr-1 dsRBD. The most notable rearrangement of the Dcr-1·Loqs-PB complex occurs upon cleavage of the 3′ arm (structure IV; Figure 6A). When both pre-miRNA arms have been cleaved, Dcr-1 undergoes partial closure (Figures 6B and S5C), accompanied by the departure of the Dcr-1 dsRBD from the cleft between the core and base. Closure narrows the

loop-binding pocket, indicating that this movement is coupled with pre-miRNA loop dissociation. Indeed, structure IV contains RNA density only for the miRNA/miRNA* duplex, suggesting that the loop dissociates before the duplex (Figure 6A). The mature duplex remains anchored to the Dcr-1 PAZ and platform domains (Figure 6C), whereas the lower part of the duplex, with its newly formed, 5′ monophosphate and two-nucleotide, 3′ overhang, is shifted ∼5 Å away from its position in the catalytically competent state found in structures IIa and IIb (Figure 6D). The duplex adopts an A-form helix conformation, indicating that cleavage of the strained pre-miRNA likely drives the duplex from the active sites. The duplex remains bound to dsRBD-1 of Loqs-PB, which loses contact with the RNase IIIa domain, but retains contact with the PAZ and wing domains (Figure 6C). This suggests that the miRNA/miRNA* duplex may be presented to AGO for loading as part of the Loqs-PB·Dcr-1 complex—this idea remains to be tested.

Thus, structure IV suggests that the release of the cleaved loop is a prerequisite for the subsequent departure of the miRNA/miRNA* duplex. The similarity between the Dcr-1 conformation in structure IV and the closed conformation of Dcr-1·Loqs-PB without RNA indicates that cleavage of both pre-miRNA arms and release of the loop shifts the equilibrium toward the original closed Dcr-1·Loqs-PB state (Figures 6A and 6B).
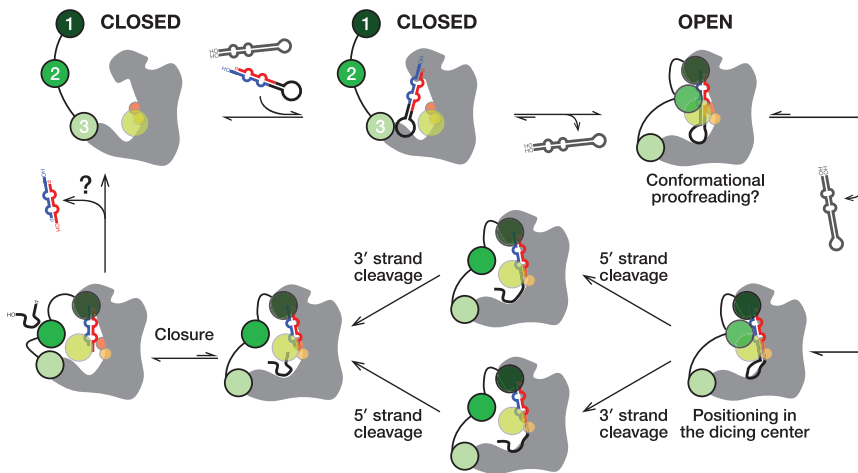
Figure 7. A model for pre-miRNA processing by the Dcr-1·Loqs-PB heterodimer without pre-miRNA, the closed conformation of the Dcr-1·Loqs-PB complex predominates

Specific interactions between an authentic pre-miRNA and the heterodimer stabilize an open, catalytically competent state. RNA hairpins lacking the pre-miRNA structural features bind weakly and dissociate without cleavage, allowing the heterodimer to return to its closed state. The Dcr-1·Loqs-PB complex envelopes the pre-miRNA. Contacts between RNA and protein residues stabilize a distorted form of pre-miRNA, docking the RNA substrate within the Dcr-1 catalytic centers. Cleavage of the 5′ and 3′ arms of pre-miRNA generates a mature miRNA/miRNA* duplex, allowing the residual loop to depart: partial closure of Dcr-1 is coupled with the release of the loop. The miRNA/miRNA* duplex remains anchored to the PAZ and platform domains of Dcr-1 and is released last.

DISCUSSION

Dicers partner with dsRBD-containing proteins in both animal and plant small RNA silencing pathways, but the mechanisms by which partner proteins enhance Dicer substrate preferences and the catalytic rate is largely unknown. Our six cryo-EM structures integrate previous structural, biochemical, and biophysical observations and suggest a parsimonious model for how Dicer and its protein partners collaborate to select and process pre-miRNAs (Figure 7).

Our cryo-EM analyses suggest that without pre-miRNA, the closed conformation of the Dicer-partner protein heterodimer predominates. By contrast, the interactions between an authentic pre-miRNA and the heterodimer stabilize an open, catalytically competent state. The opening of *Drosophila* Dcr-1·Loqs-PB upon substrate binding is consistent with the structural rearrangements that occur in the human Dicer·TRBP complex as a result of pre-*let-7* recognition (Taylor et al., 2013). Our data suggest that dsRNA or RNA hairpins lacking the structural features that define a pre-miRNA bind the Dicer-partner protein heterodimer too weakly to shift the equilibrium toward an open conformation (Figure 3G). As a result, non-pre-miRNAs are predicted to bind and depart without processing (Figure 7, far right). Supporting this idea, RNA hairpins lacking an authentic two-nucleotide 3′ overhanging end quickly dissociate from the mammalian Dicer·TRBP heterodimer (Fareh et al., 2016), and no dicing by Dcr-1 was observed for such substrates (Tsutsumi et al., 2011). Fluorescence data suggest that some substrate pre-miRNA molecules pass an "entry checkpoint," resulting in longer residency times and cleavage for Dicer·TRBP (Fareh et al., 2016). The stabilization of the Dcr-1·Loqs-PB open conformation by pre-miRNA likely represents the hypothesized checkpoint (Figure 7, top right).

Our pre-miRNA-bound structures IIa and IIb show how the Dcr-1·Loqs-PB complex recognizes pre-miRNA, forming a belt around the substrate that stabilizes the pre-miRNA in the Dcr-1 catalytic centers. The Loqs-PB dsRBD-1 and the wing domain of Dcr-1 collaborate to secure both the 5′ and 3′ pre-miRNA ends within the PAZ and platform domains of Dcr-1. The second dsRBD of Loqs-PB cooperates with the shifted dsRBD of Dcr-1 to envelop the lower part of the pre-miRNA stem in a positively charged tunnel. In this conformation, the Dcr-1 dsRBD is wedged between the protein's base and core domains, stabilizing a widened pre-miRNA loop-binding pocket in an open Dcr-1 conformation.

Since not all bound pre-miRNA undergo cleavage (Fareh et al., 2016), an additional checkpoint was proposed that converts pre-miRNA into a catalytically competent state. Our structures demonstrate that catalytically competent pre-miRNA adopts a strained conformation deviating from the A-form helix. Pre-miRNA rearrangement into this conformation likely represents the final checkpoint (Figure 7, bottom right). Together, the stabilization of the open conformation by authentic substrates and a requirement for a suboptimal—i.e., strained—substrate conformation for cleavage suggests that Dcr-1·Loqs-PB may employ conformational proofreading to evaluate the authenticity of potential dicing substrates (Savir and Tlusty, 2007).

Our structures, together with previous studies, suggest a stepwise mechanism of pre-miRNA processing by the Dcr-1·Loqs-PB heterodimer that relies on the recognition of all pre-miRNA-defining elements, from the termini to the loop. Prior to pre-miRNA binding, the closed Dcr-1 conformation features a narrow RNA-binding pocket between the core and base superdomains, and the Dcr-1 C-terminal dsRBD is bound near this pocket (structures Ia and Ib; Figure 7). In this conformation, pre-miRNA binding to the catalytic center is blocked, so it is likely that pre-accommodation states of the complex exist in which pre-miRNA is bound to Dcr-1·Loqs-PB in catalytically incompetent state(s). In one scenario, pre-miRNA may first interact with the RNA-binding Loqs-PB, which is tethered to Dcr-1 via dsRBD-3 in structures Ia and Ib (Figure 7, top center). dsRBD-1 and dsRBD-2 of Loqs-PB are not resolved, indicating that they are mobile and available to participate in the initial binding of RNA. In an alternative pathway, pre-miRNA could initially interact with the Dicer upon recognition of some specific RNA features by the protein.

Cryo-EM reconstruction of the human Dicer·TRBP complex with a model pre-miRNA is consistent with the second scenario (Liu et al., 2018). The study reported a catalytically incompetent complex conformation in which pre-miRNA termini interact with PAZ while the loop is placed ~40 Å away from its catalytically engaged position in our structures IIa and IIb. As in our closed-state structures Ia and Ib, the dsRBD of human Dicer in this catalytically incompetent conformation blocks entrance to the RNA-processing center. Because dsRBD-1 and dsRBD-2 of TRBP are not visible in the human Dicer·TRBP complex, the partner protein appears to play a key role in positioning pre-miRNA substrate for cleavage rather than participating in the initial engagement of potential RNA substrates. Some of our 2D class averages of the Dcr-1·Loqs-PB·pre-miRNA complex in presence of Ca²⁺ contain particles that resemble the human Dicer·TRBP·pre-miRNA complex. Nevertheless, they did not yield a similar 3D reconstruction, suggesting that if our dataset contains pre-accommodation states, they are rare. This suggests that if the initial engagement of Dcr-1·Loqs-PB with pre-miRNA is in a catalytically incompetent state, displacement of the Dcr-1 dsRBD and relocation of the pre-miRNA are not rate-determining for RNA processing, and Dcr-1·Loqs-PB·pre-miRNA rapidly progresses to a catalytically competent state after binding an authentic pre-miRNA substrate.

Previous studies suggested several possible mechanisms by which Dicer enzymes define small RNA length—the 3′ counting rule (Macrae et al., 2006; MacRae et al., 2007), the 5′ counting rule (Park et al., 2011), and the loop-counting rule (Gu et al., 2012). Our structures suggest that Dcr-1 recognizes both the 5′-phosphorylated nucleotide and the two-nucleotide 3′ overhang of pre-miRNA and support the model that Dicer initially combines 5′ and 3′ end recognition to measure miRNA length (Macrae et al., 2006; Park et al., 2011; Tsutsumi et al., 2011; Tian et al., 2014). The ~80 Å distance from the 3′ end binding site of the PAZ domain to the loop-binding pocket formed by Hel2, DUF283, and dsRBD is consistent with the length requirement for a pre-miRNA substrate. Furthermore, our catalytically competent structures feature an unexpected 1-nt bulge at position 36, i.e., two nucleotides downstream of the RNase IIIa active center. This observation supports the "loop-counting model," which postulates that the dicing of the 3′ strand is determined by the two-nucleotide distance between the site of cleavage and the upstream loop or bulge structure of the pre-miRNA (Gu et al., 2012). Further supporting this model, recent chemical probing of intact pre-miRNA in human cells showed that 45% of pre-miRNAs have a 3′ arm scissile phosphate that lies 2 nt away from a bulge or a loop (Luo et al., 2021).

In the cleavage-competent conformation, contacts between RNA and protein residues stabilize a distorted form of pre-miRNA in which the scissile phosphates are docked properly within the RNase IIIa and IIIb sites. Crystal structures of isolated RNase III-substrate complexes do not reveal similar RNA deviations from the A-helix geometry (Gan et al., 2008; Meng and Nicholson, 2008), suggesting that pre-miRNA distortion likely results from anchoring pre-miRNA ends in the PAZ and platform domains, docking of the pre-miRNA loop in the loop-binding region, and stabilization of the RNA stem by dsRBDs of Dcr-1 and Loqs-PB.

Pre-miRNAs with central mismatches in the stem may bind Dcr-1 but fail to undergo the conformational changes required for cleavage, resulting in unfavorably aligned nucleotides near the RNA-processing center. DsRBD-2 of Loqs-PB supports the dsRBD of Dcr-1 and increases pre-miRNA contacts with the phosphate backbone of RNA. We postulate that this duo of dsRBDs corrects the suboptimal geometry of difficult substrates by stabilizing the internal loop or cleavage site mismatches, allowing the accommodation of the pre-miRNA in the catalytic center of Dcr-1. Supporting this model, previous studies showed that pre-miRNAs containing mismatches at the center of the stem or at the cleavage sites (e.g., miR-7, miR-307, miR-311, and *bantam*) require Loqs-PB for efficient dicing (Förstemann et al., 2005; Saito et al., 2005; Fukunaga et al., 2012; Lim et al., 2016; Zhu et al., 2018). Moreover, because mismatches can change the contour length of dsRNA (Holbrook et al., 1991; Baeyens et al., 1995; Sheng et al., 2014), the stabilization of alternative pre-miRNA stem conformations by the Loqs-PB belt likely adjusts the pre-miRNA stem near the active centers, shifting the cleavage site by one or two nucleotides and leading to shorter or longer products than those made without Loqs-PB (Fukunaga et al., 2012). These results rationalize how Loqs-PB increases the binding affinity of Dcr-1 for pre-miRNA (Jiang et al., 2005) and stabilizes pre-miRNA structure for catalysis (Lim et al., 2016).

Positioning of the RNA substrate is followed by classical RNase III cleavage to generate a miRNA/miRNA* duplex and a residual loop. Dicer cleavage is unlikely to be concerted: mutations that inactivate one of the two RNase III active sites of human Dicer still allow the other active site to nick the stem on one arm (Gurtan et al., 2012). Our structure III and biochemical experiments show that Dcr-1·Loqs-PB cleaves the 5′ and 3′ arms of our model pre-miRNA sequentially. By contrast, Dcr-1·Loqs-PB cleaves the two arms of the pre-*let-7* stem at similar rates. Whether the cleavage of the 5′ and 3′ arms of the stems of authentic pre-miRNAs is typically ordered or random remains to be determined.

After cleavage (structure IV), the miRNA/miRNA* duplex remains anchored to the PAZ and platform domains of Dcr-1 (Figure 7, bottom left). The absence of density for the loop and the narrowing of the Dcr-1 loop-binding pocket indicate that the loop product has been released from the active site. The release of the loop before the duplex product likely reflects the relief of conformational strain after cleavage of the stem, as well as the paucity of stabilizing interactions between the loop and the Dcr-1 loop-binding pocket, which presents a neutral surface as opposed to the positively charged stem-binding regions of Dcr-1 and Loqs-PB. Loop release is coupled with the closure of Dcr-1 in structure IV, in keeping with the predominance of the closed Dicer conformations in the absence of pre-miRNA. The relief of the conformational strain, along with the loss of the covalent bonds between the two products, may contribute to product release. Following the release of the miRNA/miRNA* product, we envision Dcr-1·Loqs-PB closing, allowing for another round of conformational proofreading of the substrate.

Limitations of the study

Our structures were solved with a variant of pre-*let-7* in which the stem was entirely base-paired and had increased stem stability.

Future structural studies of authentic pre-miRNAs will be required to visualize how Dcr-1·Loqs-PB corrects the suboptimal geometry of some pre-miRNAs with stem or cleavage site mismatches, allowing accommodation of the pre-miRNA in the active sites of Dcr-1. These additional structural studies of various authentic substrates will also help to understand whether cleavage of the 5′ and 3′ arms of the pre-miRNA stems is typically not ordered.

STAR★METHODS

Detailed methods are provided in the online version of this paper and include the following:

- KEY RESOURCES TABLE
- RESOURCE AVAILABILITY
  - Lead contact
  - Materials availability
  - Data and code availability
- METHOD DETAILS
  - Recombinant Dcr-1 and Loqs-PB Expression and Purification
  - RNA Substrates
  - Substrate Competition Assay
  - Dicing Assay
  - In Vitro Reconstitution of the Dcr-1·Loqs-PB·Pre-miRNA Complex
  - Cryo-EM Specimen Preparation
  - Cryo-EM Data Collection for the Dcr-1·Loqs-PB Heterodimer
  - Cryo-EM Data Collection for Ternary Dcr-1·Loqs-PB·Pre-miRNA Complexes
- QUANTIFICATION AND STATISTICAL ANALYSIS
  - Dicing Assays
  - Data Processing for the Dcr-1·Loqs-PB Heterodimer
  - Data Processing for Dcr-1·Loqs-PB·Pre-miRNA with Mg^{2+}
  - Data processing for Dcr-1·Loqs-PB·Pre-miRNA with Ca^{2+}
  - Model Building and Structure Refinement

REFERENCES

Adams, P.D., Afonine, P.V., Bunkóczi, G., Chen, V.B., Davis, I.W., Echols, N., Headd, J.J., Hung, L.W., Kapral, G.J., Grosse-Kunstleve, R.W., et al. (2010). Phenix: a comprehensive Python-based system for macromolecular structure solution. Acta Crystallogr. D Biol. Crystallogr. *66*, 213–221.

Ambros, V., Bartel, B., Bartel, D.P., Burge, C.B., Carrington, J.C., Chen, X., Dreyfuss, G., Eddy, S.R., Griffiths-Jones, S., Marshall, M., et al. (2003). A uniform system for microRNA annotation. RNA *9*, 277–279.

Antczak, M., Popenda, M., Zok, T., Sarzynska, J., Ratajczak, T., Tomczyk, K., Adamiak, R.W., and Szachniuk, M. (2016). New functionality of RNAComposer: application to shape the axis of miR160 precursor structure. Acta Biochim Pol *63*.

Baeyens, K.J., De Bondt, H.L., and Holbrook, S.R. (1995). Structure of an RNA double helix including uracil-uracil base pairs in an internal loop. Nat. Struct. Biol. *2*, 56–62.

Bartel, D.P. (2018). Metazoan microRNAs. Cell *173*, 20–51.

Blaszczyk, J., Tropea, J.E., Bubunenko, M., Routzahn, K.M., Waugh, D.S., Court, D.L., and Ji, X. (2001). Crystallographic and modeling studies of RNase III suggest a mechanism for double-stranded RNA cleavage. Structure *9*, 1225–1236.

Brennecke, J., Stark, A., Russell, R.B., and Cohen, S.M. (2005). Principles of microRNA-target recognition. PLoS Biol. *3*, e85.

Campbell, F.E., Cassano, A.G., Anderson, V.E., and Harris, M.E. (2002). Pre-steady-state and stopped-flow fluorescence analysis of Escherichia coli ribonuclease III: insights into mechanism and conformational changes associated with binding and catalysis. J. Mol. Biol. *317*, 21–40.

Cenik, E.S., Fukunaga, R., Lu, G., Dutcher, R., Wang, Y., Tanaka Hall, T.M., and Zamore, P.D. (2011). Phosphate and R2D2 restrict the substrate specificity of Dicer-2, an ATP-driven ribonuclease. Mol. Cell *42*, 172–184.

Chen, S., Liu, W., Naganuma, M., Tomari, Y., and Iwakawa, H.O. (2022). Functional specialization of monocot DCL3 and DCL5 proteins through the evolution of the PAZ domain. Nucleic Acids Res. *50*, 4669–4684.

Chen, V.B., Arendall, W.B., Headd, J.J., Keedy, D.A., Immormino, R.M., Kapral, G.J., Murray, L.W., Richardson, J.S., and Richardson, D.C. (2010). MolProbity: all-atom structure validation for macromolecular crystallography. Acta Crystallogr. D Biol. Crystallogr. *66*, 12–21.

Chen, X. (2009). Small RNAs and their roles in plant development. Annu. Rev. Cell Dev. Biol. *25*, 21–44.

Chendrimada, T.P., Gregory, R.I., Kumaraswamy, E., Norman, J., Cooch, N., Nishikura, K., and Shiekhattar, R. (2005). TRBP recruits the Dicer complex to Ago2 for microRNA processing and gene silencing. Nature *436*, 740–744.

Chiang, H.R., Schoenfeld, L.W., Ruby, J.G., Auyeung, V.C., Spies, N., Baek, D., Johnston, W.K., Russ, C., Luo, S., Babiarz, J.E., et al. (2010). Mammalian microRNAs: experimental evaluation of novel and previously annotated genes. Genes Dev. *24*, 992–1009.

Court, D.L., Gan, J., Liang, Y.H., Shaw, G.X., Tropea, J.E., Costantino, N., Waugh, D.S., and Ji, X. (2013). RNase III: genetics and function; structure and mechanism. Annu. Rev. Genet. 47, 405–431.

Daniels, S.M., Melendez-Peña, C.E., Scarborough, R.J., Daher, A., Christensen, H.S., El Far, M., Purcell, D.F.J., Lainé, S., and Gatignol, A. (2009). Characterization of the TRBP domain required for Dicer interaction and function in RNA interference. BMC Mol. Biol. 10, 38. https://doi.org/10.1186/1471-2199-10-38.

Denli, A.M., Tops, B.B., Plasterk, R.H., Ketting, R.F., and Hannon, G.J. (2004). Processing of primary microRNAs by the microprocessor complex. Nature 432, 231–235.

Dong, Q., Hu, B., and Zhang, C. (2022). microRNAs and their roles in plant development. Front. Plant Sci. 13, 824240.

Emsley, P., Lohkamp, B., Scott, W.G., and Cowtan, K. (2010). Features and development of coot. Acta Crystallogr. D Biol. Crystallogr. 66, 486–501.

Evans, R., O'Neill, M., Pritzel, A., Antropova, N., Senior, A., Green, T., Žídek, A., Bates, R., Blackwell, S., Yim, J., et al. (2021). Protein complex prediction with AlphaFold-Multimer. https://doi.org/10.1101/2021.10.04.463034.

Fareh, M., Yeom, K.H., Haagsma, A.C., Chauhan, S., Heo, I., and Joo, C. (2016). TRBP ensures efficient Dicer processing of precursor microRNA in RNA-crowded environments. Nat. Commun. 7, 13694.

Förstemann, K., Horwich, M.D., Wee, L., Tomari, Y., and Zamore, P.D. (2007). Drosophila microRNAs are sorted into functionally distinct Argonaute complexes after production by Dicer-1. Cell 130, 287–297.

Förstemann, K., Tomari, Y., Du, T., Vagin, V.V., Denli, A.M., Bratu, D.P., Klattenhoff, C., Theurkauf, W.E., and Zamore, P.D. (2005). Normal microRNA maturation and germ-line stem cell maintenance requires Loquacious, a double-stranded RNA-binding domain protein. PLoS Biol. 3, e236.

Fukunaga, R., Han, B.W., Hung, J.H., Xu, J., Weng, Z., and Zamore, P.D. (2012). Dicer partner proteins tune the length of mature miRNAs in flies and mammals. Cell 151, 533–546.

Gan, J., Shaw, G., Tropea, J.E., Waugh, D.S., Court, D.L., and Ji, X. (2008). A stepwise model for double-stranded RNA processing by ribonuclease III. Mol. Microbiol. 67, 143–154.

Gleghorn, M.L., and Maquat, L.E. (2014). 'Black sheep' that don't leave the double-stranded RNA-binding domain fold. Trends Biochem. Sci. 39, 328–340.

Gregory, R.I., Yan, K.P., Amuthan, G., Chendrimada, T., Doratotaj, B., Cooch, N., and Shiekhattar, R. (2004). The microprocessor complex mediates the genesis of microRNAs. Nature 432, 235–240.

Grishok, A., Pasquinelli, A.E., Conte, D., Li, N., Parrish, S., Ha, I., Baillie, D.L., Fire, A., Ruvkun, G., and Mello, C.C. (2001). Genes and mechanisms related to RNA interference regulate expression of the small temporal RNAs that control C. elegans developmental timing. Cell 106, 23–34.

Gu, S., Jin, L., Zhang, Y., Huang, Y., Zhang, F., Valdmanis, P.N., and Kay, M.A. (2012). The loop position of shRNAs and pre-miRNAs is critical for the accuracy of dicer processing in vivo. Cell 151, 900–911.

Gurtan, A.M., Lu, V., Bhutkar, A., and Sharp, P.A. (2012). In vivo structure-function analysis of human Dicer reveals directional processing of precursor miRNAs. RNA 18, 1116–1122.

Haase, A.D., Jaskiewicz, L., Zhang, H., Lainé, S., Sack, R., Gatignol, A., and Filipowicz, W. (2005). TRBP, a regulator of cellular PKR and HIV-1 virus expression, interacts with Dicer and functions in RNA silencing. EMBO Rep. 6, 961–967.

Han, J., Lee, Y., Yeom, K.H., Kim, Y.K., Jin, H., and Kim, V.N. (2004). The Drosha-DGCR8 complex in primary microRNA processing. Genes Dev. 18, 3016–3027.

Han, J., Lee, Y., Yeom, K.H., Nam, J.W., Heo, I., Rhee, J.K., Sohn, S.Y., Cho, Y., Zhang, B.T., and Kim, V.N. (2006). Molecular basis for the recognition of primary microRNAs by the Drosha-DGCR8 complex. Cell 125, 887–901.

Hansen, S.R., Aderounmu, A.M., Donelick, H.M., and Bass, B.L. (2019). Dicer's helicase domain: a meeting place for regulatory proteins. Cold Spring Harb. Symp. Quant. Biol. 84, 185–193.

Holbrook, S.R., Cheong, C., Tinoco, I., and Kim, S.H. (1991). Crystal structure of an RNA double helix incorporating a track of non-Watson-Crick base pairs. Nature 353, 579–581.

Hubbard, S.J., and Thornton, J.M. (1993). naccess. Computer Program, Department of biochemistry and molecular Biology (University College London).

Hutvágner, G., McLachlan, J., Pasquinelli, A.E., Bálint, E., Tuschl, T., and Zamore, P.D. (2001). A cellular function for the RNA-interference enzyme Dicer in the maturation of the let-7 small temporal RNA. Science 293, 834–838.

Jakob, L., Treiber, T., Treiber, N., Gust, A., Kramm, K., Hansen, K., Stotz, M., Wankerl, L., Herzog, F., Hannus, S., et al. (2016). Structural and functional insights into the fly microRNA biogenesis factor Loquacious. RNA 22, 383–396.

Jiang, F., Ye, X., Liu, X., Fincher, L., McKearin, D., and Liu, Q. (2005). Dicer-1 and R3D1-L catalyze microRNA maturation in Drosophila. Genes Dev. 19, 1674–1679.

Dunn, J.J., and Boyer, P.D. (1982). Ribonuclease III15 (Academic Press), pp. 485–499.

Jumper, J., Evans, R., Pritzel, A., Green, T., Figurnov, M., Ronneberger, O., Tunyasuvunakool, K., Bates, R., Žídek, A., Potapenko, A., et al. (2021). Highly accurate protein structure prediction with AlphaFold. Nature 596, 583–589.

Kawamata, T., Seitz, H., and Tomari, Y. (2009). Structural determinants of miRNAs for RISC loading and slicer-independent unwinding. Nat. Struct. Mol. Biol. 16, 953–960.

Khvorova, A., Reynolds, A., and Jayasena, S.D. (2003). Functional siRNAs and miRNAs exhibit strand bias. Cell 115, 209–216.

Knight, S.W., and Bass, B.L. (2001). A role for the RNase III enzyme DCR-1 in RNA interference and germ line development in Caenorhabditis elegans. Science 293, 2269–2271.

Kremer, J.R., Mastronarde, D.N., and McIntosh, J.R. (1996). Computer visualization of three-dimensional image data using IMOD. J. Struct. Biol. 116, 71–76.

Kurzynska-Kokorniak, A., Pokornowska, M., Koralewska, N., Hoffmann, W., Bienkowska-Szewczyk, K., and Figlerowicz, M. (2016). Revealing a new activity of the human Dicer DUF283 domain in vitro. Sci. Rep. 6, 23989.

Kwon, S.C., Nguyen, T.A., Choi, Y.-G., Jo, M.H., Hohng, S., Kim, V.N., and Woo, J.-S. (2016). Structure of human DROSHA. Cell 164, 81–90.

Lai, E.C. (2002). Micro RNAs are complementary to 3′ UTR sequence motifs that mediate negative post-transcriptional regulation. Nat. Genet. 30, 363–364.

Lau, P.W., Guiley, K.Z., De, N., Potter, C.S., Carragher, B., and MacRae, I.J. (2012). The molecular architecture of human Dicer. Nat. Struct. Mol. Biol. 19, 436–440.

Lau, P.W., Potter, C.S., Carragher, B., and MacRae, I.J. (2009). Structure of the human dicer-TRBP complex by electron microscopy. Structure 17, 1326–1332.

Lee, Y., Ahn, C., Han, J., Choi, H., Kim, J., Yim, J., Lee, J., Provost, P., Rådmark, O., Kim, S., and Kim, V.N. (2003). The nuclear RNase III Drosha initiates microRNA processing. Nature 425, 415–419.

Lee, Y., Hur, I., Park, S.-Y., Kim, Y.-K., Suh, M.R., and Kim, V.N. (2006). The role of PACT in the RNA silencing pathway. EMBO J. 25, 522–532.

Lewis, B.P., Shih, I.H., Jones-Rhoades, M.W., Bartel, D.P., and Burge, C.B. (2003). Prediction of mammalian microRNA targets. Cell 115, 787–798.

Lim, M.Y., Ng, A.W., Chou, Y., Lim, T.P., Simcox, A., Tucker-Kellogg, G., and Okamura, K. (2016). The Drosophila Dicer-1 partner loquacious enhances miRNA processing from hairpins with unstable structures at the dicing site. Cell Rep. 15, 1795–1808.

Lingel, A., Simon, B., Izaurralde, E., and Sattler, M. (2003). Structure and nucleic-acid binding of the Drosophila Argonaute 2 PAZ domain. Nature 426, 465–469.

Lingel, A., Simon, B., Izaurralde, E., and Sattler, M. (2004). Nucleic acid 3′-end recognition by the Argonaute2 PAZ domain. Nat. Struct. Mol. Biol. *11*, 576–577.

Liu, Z., Wang, J., Cheng, H., Ke, X., Sun, L., Zhang, Q.C., and Wang, H.W. (2018). Cryo-EM structure of human dicer and its complexes with a pre-miRNA substrate. Cell *173*, 1191–1203.e12.

Luo, Q.J., Zhang, J., Li, P., Wang, Q., Zhang, Y., Roy-Chaudhuri, B., Xu, J., Kay, M.A., and Zhang, Q.C. (2021). RNA structure probing reveals the structural basis of Dicer binding and cleavage. Nat. Commun. *12*, 3397.

Ma, J.B., Ye, K., and Patel, D.J. (2004). Structural basis for overhang-specific small interfering RNA recognition by the PAZ domain. Nature *429*, 318–322.

MacRae, I.J., Zhou, K., and Doudna, J.A. (2007). Structural determinants of RNA recognition and cleavage by Dicer. Nat. Struct. Mol. Biol. *14*, 934–940.

Macrae, I.J., Zhou, K., Li, F., Repic, A., Brooks, A.N., Cande, W.Z., Adams, P.D., and Doudna, J.A. (2006). Structural basis for double-stranded RNA processing by Dicer. Science *311*, 195–198.

Maniataki, E., and Mourelatos, Z. (2005). A human, ATP-independent, RISC assembly machine fueled by pre-miRNA. Genes Dev. *19*, 2979–2990.

Mastronarde, D.N. (2005). Automated electron microscope tomography using robust prediction of specimen movements. J. Struct. Biol. *152*, 36–51.

Meister, G., Landthaler, M., Patkaniowska, A., Dorsett, Y., Teng, G., and Tuschl, T. (2004). Human Argonaute2 mediates RNA cleavage targeted by miRNAs and siRNAs. Mol. Cell *15*, 185–197.

Meng, W., and Nicholson, A.W. (2008). Heterodimer-based analysis of subunit and domain contributions to double-stranded RNA processing by Escherichia coli RNase III in vitro. Biochem. J. *410*, 39–48.

Moore, M.J., and Query, C.C. (2000). Joining of RNAs by splinted ligation. Methods Enzymol. *317*, 109–123.

Moore, M.J., and Sharp, P.A. (1993). Evidence for two active sites in the spliceosome provided by stereochemistry of pre-mRNA splicing. Nature *365*, 364–368.

Nicholson, A.W. (2014). Ribonuclease III mechanisms of double-stranded RNA cleavage. Wiley Interdiscip. Rev. RNA *5*, 31–48.

Okamura, K., Ishizuka, A., Siomi, H., and Siomi, M.C. (2004). Distinct roles for Argonaute proteins in small RNA-directed RNA cleavage pathways. Genes Dev. *18*, 1655–1666.

Ota, H., Sakurai, M., Gupta, R., Valente, L., Wulff, B.-E., Ariyoshi, K., Iizasa, H., Davuluri, R.V., and Nishikura, K. (2013). ADAR1 forms a complex with dicer to promote microRNA processing and RNA-induced gene silencing. Cell *153*, 575–589.

Park, J.-E., Heo, I., Tian, Y., Simanshu, D.K., Chang, H., Jee, D., Patel, D.J., and Kim, V.N. (2011). Dicer recognizes the 5′ end of RNA for efficient and accurate processing. Nature *475*, 201–205.

Partin, A.C., Zhang, K., Jeong, B.C., Herrell, E., Li, S., Chiu, W., and Nam, Y. (2020). Cryo-EM structures of human drosha and DGCR8 in complex with primary microRNA. Mol. Cell *78*, 411–422.e4.

Pettersen, E.F., Goddard, T.D., Huang, C.C., Meng, E.C., Couch, G.S., Croll, T.I., Morris, J.H., and Ferrin, T.E. (2021). UCSF ChimeraX: structure visualization for researchers, educators, and developers. Protein Sci. *30*, 70–82.

Provost, P., Dishart, D., Doucet, J., Frendewey, D., Samuelsson, B., and Rådmark, O. (2002). Ribonuclease activity and RNA binding of recombinant human Dicer. EMBO J. *21*, 5864–5874.

Punjani, A., Zhang, H., and Fleet, D.J. (2020). Non-uniform refinement: adaptive regularization improves single-particle cryo-EM reconstruction. Nat. Methods *17*, 1214–1221.

Qin, H., Chen, F., Huan, X., Machida, S., Song, J., and Yuan, Y.A. (2010). Structure of the Arabidopsis thaliana DCL4 DUF283 domain reveals a noncanonical double-stranded RNA-binding fold for protein-protein interaction. RNA *16*, 474–481.

Rohou, A., and Grigorieff, N. (2015). CTFFIND4: fast and accurate defocus estimation from electron micrographs. J. Struct. Biol. *192*, 216–221.

Saenger, W. (1984). Forces stabilizing associations between bases: hydrogen bonding and base stacking. In Principle of nucleic acids structure (Springer), pp. 116–158.

Saito, K., Ishizuka, A., Siomi, H., and Siomi, M.C. (2005). Processing of pre-microRNAs by the Dicer-1-Loquacious complex in Drosophila cells. PLoS Biol. *3*, e235.

Sassa, A., Beard, W.A., Shock, D.D., and Wilson, S.H. (2013). Steady-state, pre-steady-state, and single-turnover kinetic measurement for DNA glycosylase activity. J. Vis. Exp. *78*, e50695.

Savir, Y., and Tlusty, T. (2007). Conformational proofreading: the impact of conformational changes on the specificity of molecular recognition. PLoS One *2*, e468.

Schwarz, D.S., Hutvágner, G., Du, T., Xu, Z., Aronin, N., and Zamore, P.D. (2003). Asymmetry in the assembly of the RNAi enzyme complex. Cell *115*, 199–208.

Sheng, J., Larsen, A., Heuberger, B.D., Blain, J.C., and Szostak, J.W. (2014). Crystal structure studies of RNA duplexes containing s(2)U:A and s(2)U:U base pairs. J. Am. Chem. Soc. *136*, 13916–13924.

Sinha, N.K., Iwasa, J., Shen, P.S., and Bass, B.L. (2018). Dicer uses distinct modules for recognizing dsRNA termini. Science *359*, 329–334.

Song, J.J., Liu, J., Tolia, N.H., Schneiderman, J., Smith, S.K., Martienssen, R.A., Hannon, G.J., and Joshua-Tor, L. (2003). The crystal structure of the Argonaute2 PAZ domain reveals an RNA binding motif in RNAi effector complexes. Nat. Struct. Biol. *10*, 1026–1032.

Sun, W., Pertzev, A., and Nicholson, A.W. (2005). Catalytic mechanism of *Escherichia coli* ribonuclease III: kinetic and inhibitor evidence for the involvement of two magnesium ions in RNA phosphodiester hydrolysis. Nucleic Acids Res. *33*, 807–815.

Taylor, D.W., Ma, E., Shigematsu, H., Cianfrocco, M.A., Noland, C.L., Nagayama, K., Nogales, E., Doudna, J.A., and Wang, H.W. (2013). Substrate-specific structural rearrangements of human Dicer. Nat. Struct. Mol. Biol. *20*, 662–670.

Tian, Y., Simanshu, D.K., Ma, J.B., Park, J.E., Heo, I., Kim, V.N., and Patel, D.J. (2014). A phosphate-binding pocket within the platform-PAZ-connector helix cassette of human Dicer. Mol. Cell *53*, 606–616.

Tomari, Y., Du, T., and Zamore, P.D. (2007). Sorting of Drosophila small silencing RNAs. Cell *130*, 299–308.

Tsutsumi, A., Kawamata, T., Izumi, N., Seitz, H., and Tomari, Y. (2011). Recognition of the pre-miRNA structure by Drosophila Dicer-1. Nat. Struct. Mol. Biol. *18*, 1153–1158.

Wagner, T., Merino, F., Stabrin, M., Moriya, T., Antoni, C., Apelbaum, A., Hagel, P., Sitsel, O., Raisch, T., Prumbaum, D., et al. (2019). SPHIRE-crYOLO is a fast and accurate fully automated particle picker for cryo-EM. Commun. Biol. *2*, 218.

Wagner, T., and Raunser, S. (2020). The evolution of SPHIRE-crYOLO particle picking and its application in automated cryo-EM processing workflows. Commun. Biol. *3*, 61.

Wang, H.-W., Noland, C., Siridechadilok, B., Taylor, D.W., Ma, E., Felderer, K., Doudna, J.A., and Nogales, E. (2009). Structural insights into RNA processing by the human RISC-loading complex. Nat. Struct. Mol. Biol. *16*, 1148–1153.

Wang, Q., Xue, Y., Zhang, L., Zhong, Z., Feng, S., Wang, C., Xiao, L., Yang, Z., Harris, C.J., Wu, Z., et al. (2021). Mechanism of siRNA production by a plant Dicer-RNA complex in dicing-competent conformation. Science *374*, 1152–1157.

Watkins, A.M., Rangan, R., and Das, R. (2020). FARFAR2: improved de novo Rosetta prediction of complex global RNA folds. Structure *28*, 963–976.e6.

Wei, X., Ke, H., Wen, A., Gao, B., Shi, J., and Feng, Y. (2021). Structural basis of microRNA processing by Dicer-like 1. Nat. Plants *7*, 1389–1396.

Wilson, R.C., Tambe, A., Kidwell, M.A., Noland, C.L., Schneider, C.P., and Doudna, J.A. (2015). Dicer-TRBP complex formation ensures accurate mammalian microRNA biogenesis. Mol. Cell *57*, 397–407.

Xia, T., Santalucia, J., Burkard, M.E., Kierzek, R., Schroeder, S.J., Jiao, X., Cox, C., and Turner, D.H. (1998). Thermodynamic parameters for an expanded nearest-neighbor model for formation of RNA duplexes with Watson−Crick base pairs. Biochemistry *37*, 14719–14735.

Yan, K.S., Yan, S., Farooq, A., Han, A., Zeng, L., and Zhou, M.M. (2003). Structure and conserved RNA binding of the PAZ domain. Nature *426*, 468–474.

Yang, S.W., Chen, H.Y., Yang, J., Machida, S., Chua, N.H., and Yuan, Y.A. (2010). Structure of Arabidopsis HYPONASTIC LEAVES1 and its molecular implications for miRNA processing. Structure *18*, 594–605.

Ye, X., Paroo, Z., and Liu, Q. (2007). Functional anatomy of the Drosophila microRNA-generating enzyme. J. Biol. Chem. *282*, 28373–28378.

Zapletal, D., Taborska, E., Pasulka, J., Malik, R., Kubicek, K., Zanova, M., Much, C., Sebesta, M., Buccheri, V., Horvat, F., et al. (2022). Molecular basis of indispensable accuracy of mammalian miRNA biogenesis. Mol. Cell *82*, 4064–4079.

Zhang, H., Kolb, F.A., Jaskiewicz, L., Westhof, E., and Filipowicz, W. (2004). Single processing center models for human Dicer and bacterial RNase III. Cell *118*, 57–68.

Zhang, L., Xiang, Y., Chen, S., Shi, M., Jiang, X., He, Z., and Gao, S. (2022). Mechanisms of microRNA biogenesis and stability control in plants. Front. Plant Sci. *13*, 844149.

Zheng, S.Q., Palovcak, E., Armache, J.P., Verba, K.A., Cheng, Y., and Agard, D.A. (2017). MotionCor2: anisotropic correction of beam-induced motion for improved cryo-electron microscopy. Nat. Methods *14*, 331–332.

Zhu, L., Kandasamy, S.K., and Fukunaga, R. (2018). Dicer partner protein tunes the length of miRNAs using base-mismatch in the pre-miRNA stem. Nucleic Acids Res. *46*, 3726–3741.

Zivanov, J., Nakane, T., Forsberg, B.O., Kimanius, D., Hagen, W.J., Lindahl, E., and Scheres, S.H. (2018). New tools for automated high-resolution cryo-EM structure determination in RELION-3. eLife *7*, e42166.

STAR★METHODS

KEY RESOURCES TABLE

REAGENT or RESOURCE	SOURCE	IDENTIFIER
Chemicals, peptides, and recombinant proteins		
Bac-to-Bac Baculovirus Expression system	ThermoFisher	10359016
SFX-Insect liquid medium with L-glutamine, sodium bicarbonate	Cytiva	SH30278.LS
Penicillin-Streptomycin	Sigma-Aldrich	P0781
Critical commercial assays		
HisTrap HP 5 ml	Fisher Scientific	45000325
HiTrap Q HP 5 ml	Fisher Scientific	45000194
HiTrap Heparin 1 ml	Fisher Scientific	45000057
HiTrap Phenyl HP 1 ml	Sigma Aldrich	GE17-1351-01
C-flat Holey Carbon Grids CF-1.2/ 1.3 400 Mesh	Electron Microscopy Sciences	CF413-50
Ultrathin Carbon Film on Lacey Carbon Support Film, 300 mesh, Gold	Ted Pella	01824G
Deposited data		
Structure Ia	This study	PDB: 8DGI
Structure Ib	This study	PDB: 8DGJ
Structure IIa	This study	PDB: 8DFV
Structure IIb	This study	PDB: 8DG5
Structure III	This study	PDB: 8DG7
Structure IV	This study	PDB: 8DGA
Experimental models: Cell lines		
Sf9 cells	ATCC	CRL-1711; RRID:CVCL_0549
Oligonucleotides		
Model pre-miRNA: 5'-UGA GGU AGU AGG UUG UAU AGU AGU AAU UAC ACA UCA UAC UAU ACA ACC UAC UAC CUC UCU-3'	Sigma	N/A
pre-*let-7*: 5'-pUGA GGU AGU AGG UUG UAU AGU AGU AAU UAC ACA UCA UAC UAU ACA AUG UGC UAG CUU UCU-3'	IDT	N/A
pre-*let-7* blunt: 5'-pUGA GGU AGU AGG UUG UAU AGU AGU AAU UAC ACA UCA UAC UAU ACA AUG UGC UAG CUU A-3'	IDT	N/A
pre-*let-7* 2-nt, 5' overhang: 5'-pAGU GAG GUA GUA GGU UGU AUA GUA GUA AUU ACA CAU CAU ACU AUA CAA UGU GCU AGC UUU-3'	IDT	N/A
pre-*let-7* 4-nt loop: 5'-pUGA GGU AGU AGG UUG UAU AGU AGA CAU ACU AUA CAA UGU GCU AGC UUU CU-3'	IDT	N/A
pre-*let-7* 20-nt loop: 5'-pUGA GGU AGU AGG UUG UAU AGU AGU AAA UCU UAC ACA UCA UCA UAC UAU ACA AUG UGC UAG CUU UCU-3'	IDT	N/A
pre-*let-7*-like (–47.2 kcal/mol): 5'-pUGA GGU AGU AGG UUG AGU CGC AGU AAU UAC ACA UCA UGC GAC UCA ACC UAC UAC CUC UCU-3'	IDT	N/A

Continued

REAGENT or RESOURCE	SOURCE	IDENTIFIER
pre-*let-7*-like (−51.2 kcal/mol): 5'-pUGA GGU AGG UUG AGG CGC GGU AAU UAC ACA UCA CGC GCC UCA ACC UAC UAC CUC UCU-3'	IDT	N/A
pre-*let-7*-like (−58.0 kcal/mol): 5'-pUGA GGU AGU AGG UUG AGG CGC GGC AAU UAC ACA AGC CGC GCC UCA ACC UAC UAC CUC UCU-3'	IDT	N/A
pre-*let-7* 38-nt RNA (let-7 and loop): 5'-UGA GGU AGU AGG UUG UAU AGU AGU AAU UAC ACA UCA UA-3'	IDT	N/A
*let-7**: 5'-CUA UAC AAU GUG CUA GCU UUC U-3'	IDT	N/A
split DNA for pre-*let-7*: 5'-GCA CAT TGT ATA GTA TGA TGT GTA ATT AC-3'	IDT	N/A
model pre-miRNA 38-nt RNA (miRNA and loop): 5'-CUA UAC AAC CUA CUA CCU CUC U-3'	IDT	N/A
split DNA for model pre-miRNA: 5'-GTA GGT TGT ATA GTA TGA TGT GTA ATT AC-3'	IDT	N/A
EcoRI Dcr-1 His6-tag sense strand: 5'-AAT TAT GCA TCA TCA CCA CCA TCA CC-3'	IDT	N/A
EcoRI Dcr-1 His6-tag antisense strand: 5'-AAT TGG TGA TGG TGG TGA TGA TGC AT-3'	IDT	N/A
EcoRI Loqs-PB His6-tag sense strand: 5'-CAC CGA ATT CAT GCA TCA CCA TCA CCA TCA CGA CCA GGA GAA TTT CCA CGG-3'	IDT	N/A
Not1 Loqs-PB antisense strand: 5'-CCA GCT GCG GCC GCT ACT TCT TGG TCA TGA TCT TC-3'	IDT	N/A
Software and algorithms		
SerialEM	Mastronarde, 2005	https://bio3d.colorado.edu/SerialEM/
Relion v3	Zivanov et al., 2018	https://github.com/3dem/relion
crYOLO 1.7.6	Wagner et al., 2019	https://github.com/MPI-Dortmund/cryolo
Pretrained crYOLO General Model	Wagner et al., 2019	ftp://ftp.gwdg.de/pub/misc/sphire/crYOLO-GENERAL-MODELS/gmodel_phosnet_202005_nn_N63_c17.h5
JANNI	Wagner and Raunser, 2020	https://github.com/MPI-Dortmund/sphire-janni
Pretrained JANNI General Model	Wagner and Raunser, 2020	https://github.com/MPI-Dortmund/sphire-janni/raw/master/janni_general_models/gmodel_janni_20190703.h5
ChimeraX	Pettersen et al., 2021	https://www.cgl.ucsf.edu/chimerax/cgi-bin/secure/chimerax-get.py?file=current/ubuntu-20.04/chimerax-daily.deb
cryoSPARC v3.3.1	Punjani et al., 2020	https://cryosparc.com/download
IMOD	Kremer et al., 1996	https://bio3d.colorado.edu/imod/
MotionCor2 v1.4.2	Zheng et al., 2017	https://emcore.ucsf.edu/ucsf-software
CTFFIND4	Rohou and Grigorieff, 2015	https://grigorefflab.umassmed.edu/ctffind4
AlphaFold	Jumper et al., 2021	https://github.com/deepmind/alphafold
AlphaFold-Multimer	Evans et al., 2021	https://github.com/deepmind/alphafold
Coot	Emsley et al., 2010	http://www2.mrc-lmb.cam.ac.uk/personal/pemsley/coot/
FARFAR2	Watkins et al., 2020	https://rosie.graylab.jhu.edu/farfar2/
RNAComposer	Antczak et al., 2016	https://rnacomposer.cs.put.poznan.pl/
Phenix	Adams et al., 2010	https://www.phenix-online.org
MolProbity	Chen et al., 2010	http://molprobity.biochem.duke.edu/index.php
NACCESS	Hubbard et al., 1993	http://www.bioinf.manchester.ac.uk/naccess/
PyMol 2.5.2	Schrödinger, Inc.	https://pymol.org

RESOURCE AVAILABILITY

Lead contact

Further information and requests for resources and reagents should be directed to, and will be fulfilled by, the lead contact, Phillip D. Zamore (phillip.zamore@umassmed.edu), or by completing the request form at https://www.zamorelab.umassmed.edu/reagents.

Materials availability

Plasmids and strains generated in this study are available for non-commercial use upon request without restriction.

Data and code availability

- The RSCB codes of the structures reported in this paper are 8DGI (structure Ia), 8DGJ (structure Ib), 8DFV (structure IIa), 8DG5 (structure IIb), 8DG7 (structure III), and 8DGA (structure IV).
- This paper does not report original code.
- Any additional information required to reanalyze the data reported in this paper is available from the lead contact upon request.

METHOD DETAILS

Recombinant Dcr-1 and Loqs-PB Expression and Purification

Sf9 cells were maintained in suspension in SFX-Insect serum-free media (HyClone Laboratories) with Penicillin (100 U/ml)-Strepto-mycin (0.1 mg/ml) (Sigma) at 27°C. His$_6$-Dcr-1 and His$_6$-Loqs-PB were co-expressed in Sf9 cells using the BAC-to-BAC Baculovirus Expression System (Invitrogen). Sf9 cells were co-infected with His$_6$-Dcr-1 (multiplicity of infection (MOI) 5) and His$_6$-Loqs-PB (MOI 2.5) viral stocks and incubated for 80–90 h at 27°C. Cells were pelleted at 500 × *g* and stored at –80°C until use. Cells were thawed on ice and re-suspended with ice-cold buffer containing 30 mM HEPES-NaOH, pH 7.4, 300 mM NaCl, 10% (w/v) glycerol, 20 mM Imid-azole, 2 mM DTT, 1 mM AEBSF, hydrochloride, 0.3 μM Aprotinin, 40 μM Bestatin, hydrochloride, 10 μM E-64, 10 μM Leupeptin hemi-sulfate, and then lysed on ice with a Dounce homogenizer using 40 strokes of a tight pestle (B type). The homogenate was centrifuged at 500 × *g* to remove nuclei and cell membranes, then at 100,000 × *g* for 20 min at 4°C.

All chromatography was conducted at 4°C. The S100 supernatant was loaded onto a column packed with 5 ml Ni-Sepharose (GE Healthcare). The column was washed with 50 ml wash buffer (30 mM HEPES-NaOH, pH 7.4, 300 mM NaCl, 10% (w/v) glycerol, 2 mM DTT) containing 20 mM imidazole, then with 50 ml wash buffer containing 40 mM Imidazole. The Dcr-1·Loqs-PB complex was eluted with 30 ml wash buffer containing 500 mM imidazole. Fractions containing Dcr-1·Loqs-PB were pooled, adjusted to 30 mM HEPES-NaOH, pH 7.4, 100 mM NaCl, 10% (w/v) glycerol, 2 mM EDTA, 2 mM DTT, and loaded onto a column packed with 5 ml Q Sepharose (GE Healthcare). The column was washed with 50 ml of column buffer (30 mM HEPES-NaOH, pH 7.4, 10% (w/v) glycerol, 2 mM EDTA, 2 mM DTT) containing 100 mM NaCl, then with 30 ml column buffer containing 200 mM NaCl. Dcr-1·Loqs-PB complex was eluted with column buffer containing 450 mM NaCl. Fractions containing Dcr-1·Loqs-PB were pooled and diluted 4.5-fold with 20 mM HEPES-NaOH, pH 7.0, 10% (w/v) glycerol, 2 mM EDTA, 2 mM DTT, to reduce the NaCl concentration to 100 mM. The sample was loaded onto a column packed with 1 ml Heparin Sepharose (GE Healthcare). The column was washed with 10 ml of 20 mM HEPES-NaOH, pH 7.0, 100 mM NaCl, 10% (w/v) glycerol, 2 mM EDTA, 2 mM DTT, then with 20 mM HEPES-NaOH, pH 7.0, 100 mM NaCl, 10% (w/v) glycerol, 2 mM EDTA, 2 mM DTT, 1 mM ATP. Dcr-1·Loqs-PB was eluted with 20 mM HEPES-NaOH, pH 7.0, 400 mM NaCl, 10% (w/v) glycerol, 2 mM EDTA, 2 mM DTT. Fractions containing Dcr-1·Loqs-PB were pooled, adjusted to 20 mM HEPES, pH 7.0, 1.5 M NaCl, 10% (w/v) glycerol, 2 mM DTT, and loaded onto a column packed with 1 ml Phenyl agarose (GE Healthcare). The column was washed with 10 ml of buffer A (20 mM HEPES, pH 7.0, 10% (w/v) glycerol, 2 mM DTT) containing 1.5 M NaCl. Dcr-1·Loqs-PB was eluted with a 30 ml linear gradient from 1.5 M to 0 M NaCl in buffer A. Fractions containing Dcr-1·Loqs-PB were pooled together and dialyzed at 4°C against three changes (3 h each) of a 1,000-fold excess of 20 mM HEPES-KOH, pH 7.9, 100 mM KCH$_3$CO$_2$, 5% (w/v) glycerol, 2 mM DTT. Immediately before preparing grids, the complex was diluted pro-gressively with 20 mM HEPES-KOH, pH 7.9, 100 mM KCH$_3$CO$_2$, 0.1% (w/v) glycerol, 2 mM TCEP, in five steps to reduce the glycerol concentration to 0.1% (w/v) and then reconcentrated with a 30 kDa cut-off Amicon Ultra centrifugal filter (Millipore) to 3 μM final concentration.

RNA Substrates

RNAs for dicing assays (Table S2, Integrated DNA Technologies) were 5′ ^{32}P radiolabeled using [γ-^{32}P]ATP (6000 Ci/mmol) (PerkinElmer, Waltham, MA) and T4 polynucleotide kinase (NEB, Ipswich, MA), and then gel-purified. Substrates containing two ^{32}P-radiolabeled phosphates were prepared by DNA-splinted ligation (Moore and Sharp, 1993; Moore and Query, 2000). Synthetic hairpins for substrate competition assays (Table S2) were ordered from Integrated DNA Technologies as HPLC-purified RNAs.

Substrate Competition Assay

Dcr-1·Loqs-PB (5 nM) was incubated in a 6-μl reaction containing 25 nM 5′ ^{32}P-radiolabled pre-*let-7*, increasing concentrations of hairpin RNAs (0–10 μM), 30 mM HEPES-NaOH, pH 7.5, 100 mM NaCl, 3 mM MgCl$_2$, and 2 mM DTT at 25°C for 15 min. Reactions

were assembled on ice and preincubated at 25°C for 5 min before adding RNA. Reactions were stopped by the addition of 60 μl urea loading buffer (7 M Urea, 25 mM EDTA, 0.1% w/v bromophenol blue), incubated for 5 min at 95°C and analyzed by electrophoresis through a denaturing 12% polyacrylamide 7 M urea gel using 0.5× Tris-borate-EDTA buffer. Gels were dried, exposed to a storage phosphor screen, and imaged on a Typhoon FLA 7000 (GE).

Dicing Assay

Dicing reactions contained 30 mM HEPES-NaOH, pH 7.5, 100 mM NaCl, 3 mM MgCl$_2$, and 2 mM DTT. Reactions were assembled on ice and preincubated at 25°C for 5 min before adding RNA. In Figures 4G and S7C, reactions contained 4 nM Dcr-1·Loqs-PB and 16 nM hairpin RNA. In Figures 5D and 5E, reactions contained 5 nM Dcr-1·Loqs-PB and 45 nM hairpin RNA. At the indicated times, an aliquot of a master reaction was quenched in four volumes 50 mM Tris-HCl, pH 7.5, 100 mM NaCl, 25 mM EDTA, 1% (w/v) SDS, then proteinase K (1 mg/ml f.c.) was added and incubated at 45°C for 15 min.

Next, RNA was ethanol-precipitated, resuspended in formamide loading buffer (98% v/v formamide, 0.1% w/v bromophenol blue and xylene cyanol, 10 mM EDTA), incubated for 5 min at 95°C and analyzed by electrophoresis through a denaturing polyacrylamide 7 M urea gel using 0.5× Tris-borate-EDTA buffer. Gels were dried, exposed to a storage phosphor screen, and imaged on a Typhoon FLA 7000 (GE). We note that the high stability of the nicked hairpin comprising radiolabeled miRNA* and radiolabeled 38-nt RNA was too high to fully denature, causing the the purified, doubly radiolabeled model pre-miRNA to be partially contaminated with the 38-nt RNA.

In Vitro Reconstitution of the Dcr-1·Loqs-PB·Pre-miRNA Complex

The model pre-miRNA corresponded to pre-*let-7* with a fully complementary stem (5′-UGA GGU AGU AGG UUG UAU AGU AGU AAU UAC ACA UCA UAC UAU ACA ACC UAC UAC CUC UCU-3′; Sigma). Pre-miRNA was 5′-phosphorylated and gel-purified. Purified Dcr-1·Loqs-PB complex was diluted to 1 μM in 20 mM HEPES-KOH, pH 7.9, 100 mM KCH$_3$CO$_2$, 0.1% (w/v) glycerol, 2 mM TCEP and 3 μM either Ca(CH$_3$CO$_2$)$_2$ or Mg(CH$_3$CO$_2$)$_2$. RNA was added in two-fold molar excess over heterodimer. To preserve protein-RNA interactions and inhibit dicing, Dcr-1·Loqs-PB·pre-miRNA complex was assembled in the presence of Ca^{2+} on ice for 1 h. To enable dicing, all components were pre-warmed to 25°C and Dcr-1·Loqs-PB·pre-miRNA complex was assembled in the presence of Mg^{2+} at 25°C for 5 min.

Cryo-EM Specimen Preparation

Fresh Dcr-1·Loqs-PB and Dcr-1·Loqs-PB·pre-miRNA complexes were purified immediately before preparing the frozen-hydrated grids. Holey-carbon grids (C-flat Holey Carbon Grids CF-1.2/1.3 400 mesh, Electron Microscopy Sciences) were glow discharged at 20 mA with negative polarity for 60 s in a PELCO easiGlow glow discharge unit. A drop of 2.5 μl (Dcr-1·Loqs-PB complex) or 3 μl (Dcr-1·Loqs-PB·pre-miRNA complex) sample was applied to the grids. Grids were blotted at blotting force 10 for 5 s at 4°C (Dcr-1·Loqs-PB), or at blotting force 10 for 5 s at 4°C (Dcr-1·Loqs-PB·pre-miRNA in presence of Ca^{2+}) or at 25°C (Dcr-1·Loqs-PB·pre-miRNA in presence of Mg^{2+}). Grids were blotted at 100% humidity and plunged into liquid ethane using a Vitrobot MK4 (FEI). Grids were stored in liquid nitrogen.

Cryo-EM Data Collection for the Dcr-1·Loqs-PB Heterodimer

A data set of 2,849 movies was collected for the Dcr-1·Loqs-PB complex on a Talos Arctica microscope operating at 200 kV (UMass Chan Medial School Cryo-EM Center). Images were recorded using the defocus range from −0.5 to −3.0 μm on a K3 Summit direct electron detector (Gatan), using SerialEM (Mastronarde, 2005) Each exposure was acquired with continuous frame streaming at 30 frames per 1.618 s yielding a total dose of 48.06 e⁻/Å^2. The nominal magnification was 45,000 and the calibrated super-resolution pixel size at the specimen level was 0.435 Å.

Cryo-EM Data Collection for Ternary Dcr-1·Loqs-PB·Pre-miRNA Complexes

Cryo-EM data sets were collected on a Titan Krios electron microscope (FEI) operating at 300 kV, equipped with a Gatan Image Filter (GIF; UMass Chan Medial School Cryo-EM Center). Images were recorded using the defocus range from −0.5 to −3.5 μm in the super-resolution mode of the K3 Summit direct electron detector (Gatan). During multi-shot data collection, data were recorded from two holes at a time, using SerialEM as described above. Magnifications for the native and Ca^{2+}-inhibited reactions were 105,000 and 81,000, yielding the super-resolution pixel sizes of 0.415 Å and 0.53 Å, respectively. For the native reaction supplemented with Mg^{2+}, a total of 8,128, 38-frame movies were recorded from two grids, with an electron dose rate of 1.75 e⁻/Å^2/frame and exposure time of 1.89 s, totaling 66.3 e⁻/Å^2. For the reaction with Ca^{2+}, 3,056, 40-frame movies were collected with an electron dose rate of 1.64 e⁻/Å^2/frame and exposure time of 2.8 s, a total dose of 65.5 e⁻/Å^2.

QUANTIFICATION AND STATISTICAL ANALYSIS

Dicing Assays

Fiji software was used to quantify the substrate and product bands in the raw image file and to correct for background. To determine IC$_{50}$ values in substrate competition assays, product formed as a function of competitor concentrations was fit to a three-parameter inhibition model:

$$y(x) = y_{max} + \frac{y_{min} - y_{max}}{1 + IC_{50}/x}$$

To determine rates of reaction, product formed as a function of time was fit to the burst-and-steady-state equation:

$$y(x) = E_{active} \times \left[(k_2/(k_2 + k_3))^2 \times \left(1 - e^{-t \times (k_2 + k_3)}\right) + t \times k_2 \times k_3 \Big/ (k_2 + k_3) \right]$$

The time-dependence of product formation corresponded to a pre-steady-state exponential burst ($k_{burst} = k_2 + k_3$) followed by a linear steady-state phase, described by k_{cat}, where $k_{cat} = k_2 \times k_3/(k_2 + k_3)$. The size of the burst corresponds to concentration of active enzyme, E_{active}.

Data Processing for the Dcr-1·Loqs-PB Heterodimer

Preliminary data analysis was done in Relion 3 (beta version) (Zivanov et al., 2018), including motion-correction summing to pixel size of 0.87 Å and CTF estimation on 2,849 movies. Particle picking with crYOLO/JANNI (Wagner et al., 2019; Wagner and Raunser, 2020) using default pretrained neural network models for denoising and picking yielded 345,112 coordinates. Particles were extracted from micrographs as a 4× binned stack with the pixel size of 3.48 Å, and the stack was subjected to 2D classification in Relion into 300 classes. Particles from Dicer-like containing classes were used to generate an *ab initio* 3D map that was smoothed using the gaussian filter implemented in ChimeraX (Pettersen et al., 2021), and the 3D map was used for template particle picking in the next step.

All 2,849 movies were patch motion-corrected without Fourier cropping as implemented in cryoSPARC v3 (Punjani et al., 2020). After the "Patch CTF" estimation, images with excessive total motion of the sample or CTF fit lower than 10 Å were removed, and further processing was done on 2,780 micrographs. The *ab initio* map obtained using Relion was used to create 50 equally spaced 2D templates, and both templates and micrographs were low-pass-filtered to 16-Å resolution. Template particle picking with the particle diameter set to 180 Å and the minimal separation distance set to 90 Å, yielded 1,478,681 particles, which were extracted as 98-px boxes with pixel size 5.2 Å. This set of particles was subjected to 2D classification into 200 classes using a 200-Å circular mask. After discarding particles that belonged to low-resolution or non-particle classes, 654,052 particles were re-extracted as a new stack with the box size of 160 px and the pixel size of 1.74 Å, and the particles were subjected to 2D classification into 80 classes. After discarding lowest-resolution and featureless classes, 615,013 particles were exported for the further analysis as two separate stacks with the pixel sizes of 0.87 Å and 3.48 Å. We performed two independent 3D classifications of the 3.48 Å/px stack into 10 classes with two types of masks. First, classification with a general 3D mask on the heterodimer revealed positional flexibility of the head relative to the core and base. Second, classification using a 33-Å radius mask covering dsRBD of Dcr-1 revealed different features of dsRBD density, suggesting conformational heterogeneity of dsRBD near its binding sites in maps Ia and Ib, where dsRBD density was most interpretable. Particles corresponding to classes Ia and Ib also featured the best resolved linker between RNase IIIb and dsRBD. They were selected from the stack of pixel size 0.87 Å as 91,617- and 112,398-particle substacks, and were subjected to non-uniform refinement in cryoSPARC resulting in 4.0-Å and 3.9-Å final maps.

Data Processing for Dcr-1·Loqs-PB·Pre-miRNA with Mg^{2+}

The data set from the first grid, containing 4,015 movies, was aligned in IMOD (Kremer et al., 1996) with the gain reference producing image sums with pixel size 0.83 Å. After inspection, 149 aligned images were discarded due to poor quality. Aligned 4×-binned images were denoised using the noise2noise algorithm implemented in JANNI (Wagner and Raunser, 2020) and used for initial particle picking with crYOLO (Wagner et al., 2019) with the pretrained general model, using box size 140 Å. After selecting 134,417 particle coordinates, all subsequent processing steps were performed in Relion (Zivanov et al., 2018). A 4×-binned particle stack with the pixel size of 3.32 Å was extracted from 3,866 motion-corrected and CTF-estimated micrographs, and template-free 2D classification into 168 classes was performed. Particles from nine, high-resolution classes totaling 57,184 particles were used to calculate an *ab initio* 3D map that was auto-refined using a mask against the same stack until 6.64 Å Nyquist-limit resolution. The resulting map revealed pre-miRNA bound to Dcr-1 with additional density that was attributed to one of the Loqs domains bound to pre-miRNA. This map was low-pass filtered to 20 Å, and with 30° angular sampling, 48 2D reprojections were generated as reference images for template-based particle picking.

For template-based particle picking, 8,128 movies from both grids were motion-corrected with a GPU-accelerated version of MotionCor2 (Zheng et al., 2017) to the final pixel size of 0.83 Å and defocus values were determined using CTFFIND4 (Rohou and Grigorieff, 2015). After discarding poor-quality micrographs, 7,895 aligned images were used for template-based particle picking, yielding a 3,161,540-particle stack. Boxes (360 px × 360 px) with particle coordinates were extracted as a 4×-binned stack with pixel size 3.32 Å, which was subjected to reference-free 2D classification into 386 classes for 30 iterations. Fourteen non-junk 2D classes accounted for 1,148,974 particles, which were selected for another round of 2D classification into 60 classes for 35 iterations to further improve the alignment parameters and to discard lower-quality particles. Sixteen 2D classes comprising 565,607 particles were selected for the masked 3D auto-refinement to calculate the updated 3D map. The refinement was performed with a starting map low-pass filtered to 30 Å, using a 10-Å hard-edge and a 10-Å soft-edge mask and converging to the final Nyquist-limit resolution of 6.64 Å.

The particle stack was 3D-classified using the updated 3D map low-pass filtered to 15 Å as a mask. Classification into six classes revealed two high-quality classes that differed in the region corresponding to pre-miRNA loop, however the remaining classes suggested unresolved conformational heterogeneity necessitating additional classification (described below). One of the two classes featured strong RNA-loop density, whereas the second class contained no density in the corresponding region. Particles from both classes were re-extracted as separate 1× stacks comprising 185,002 and 106,904 particles, and the stacks refined in cryo-SPARC to result in final maps IIa and IV at 3.3- and 4.0-Å resolutions, respectively.

To additionally resolve the heterogeneity and potentially separate the cleavage intermediates, we performed 3D classification of the 4×-binned stack into 10 classes without alignment with a 33-Å 3D mask centered at the RNase IIIb cleavage site (near pre-miRNA nucleotide 22). An additional well-resolved class was obtained that featured continuous density for the post-cleavage site fragment of the 3′ strand but not for the 5′ strand. Particles (135,303) were re-extracted into a 1× stack and refined in cryoSPARC with non-uniform refinement to result in map-III at 3.3-Å resolution.

Data processing for Dcr-1·Loqs-PB·Pre-miRNA with Ca^{2+}

Movies were motion-corrected with the GPU accelerated version of MotionCor2 (Zheng et al., 2017) to the final pixel size of 1.06 Å, and defocus values were determined using CTFFIND4 (Rohou and Grigorieff, 2015) The best 2,999 aligned images were selected for further analysis. Forty-eight 2D reprojections from Gaussian low-pass filtered map to 20 Å from our previous reconstruction were used for template-based particle picking, yielding 2,023,692 particles. Boxes (282 px × 282 px) with particle coordinates were extracted into a 3×-binned stack with pixel size 3.18 Å and subjected to reference-free 2D classification into 386 classes for 20 iterations. The six most well-resolved 2D classes representing different particle orientations were selected, totaling 1,109,821 particles. A 3D classification into six classes with a low-pass filtered (20 Å resolution) *de novo* 3D reconstruction as a reference was used to select particles with the highest-resolution features. Particles (353,726) were re-extracted with box size 340 px × 340 px with re-centering and were resampled to pixel size 1.24 Å to speed up subsequent processing steps. After masked auto-refinement, CTF-refinement and Bayesian particle polishing were performed, each followed by a round of auto-refinement and postprocessing, resulting in a 3.3 Å reconstruction.

To further improve the quality of the reconstruction, the 353,726-particle stack with pixel size 1.24 Å was 3D classified without alignment into six classes, using a 3D mask created from the previous reconstruction that was low-pass filtered to 15 Å resolution and to which 3 px of hard and soft edges were added. The highest-resolution class comprised 149,443 particles that were re-extracted as a 1.06 Å/px stack and subjected to non-uniform refinement in cryoSPARC, yielding the final 3.0 Å map corresponding to structure IIa.

Model Building and Structure Refinement

A locally installed AlphaFold version (Jumper et al., 2021) was used to obtain the starting models of Dcr-1 and Loqs-PB. AlphaFold-Multimer (Evans et al., 2021) was used to co-fold the heterodimer of Dcr-1 helicase domains (aa 1–615) with the third dsRBD domain of Loqs-PB (aa 320–465). Dcr-1 and Loqs-PB models were rigid-body refined against the maps in ChimeraX (Pettersen et al., 2021) and COOT (Emsley et al., 2010). To this end, twelve Dcr-1 domain fragments and three Loqs-PB domains were fitted independently. Pre-miRNA nucleotides 1–24 and 34–60 were modeled in COOT, using map-IIa. Since the lower-resolution density for the RNA loop did not allow for unambitious nucleotide placement, a FARFAR2-predicted (Watkins et al., 2020) starting model of the loop was generated. After the initial model building, structures of Dcr-1·Loqs-PB (Ia and Ib) and Dcr-1·Loqs-PB·pre-miRNA (IIa, IIb, III, and IV) were refined in Phenix (Adams et al., 2010) using secondary-structure restraints, and the quality of the resulting structures was assessed with MolProbity (Chen et al., 2010). The total buried surface areas at the protein-protein or protein-RNA interfaces were calculated with NACCESS (Hubbard and Thornton, 1993). Figures were prepared with PyMol (https://pymol.org).